A review of high nanoparticles concentration composites: semiconductor and high refractive index materials

Igor Yu. Denisyuk

Doctor of Science, professor, head of the chair of Quantum Sized Optical Systems of State University of Information Technologies, Mechanics and Optics Russia, 197101, Saint-Petersburg, Str. Kronverskii 49

Mari Iv. Fokina

Assistant professor of State University of Information Technologies, Mechanics and Optics Russia, 197101, Saint-Petersburg, Str. Kronverskii 49

1. Introduction

At the present time homogeneous optical and optoelectronic media such as glasses, monocrystals and polymer materials are widely used. Each of these media has a specific set of properties. For example, the polymer materials allow producing flexible and transparent films, for example film OLED. They are cheap. The technology of polymers treatment is very simple and suitable for some applications. However the holes and electrons mobility in polymer materials are many time less in comparison with inorganic well known semiconductors. Another problem is a relative high exciton decay energy in polymer with value of 100 meV that result on temperature dependence of photogeneration.

The possibility of combining the different properties into a single material should be rather useful. It is impossible to solve this problem by traditional ways because the properties reflect the internal structures of these different materials.

The method of nanostructuring provides the possibility of combining the properties of polymers and crystals. The resulting nanocomposite is the mechanical mixture of inorganic semiconductor distributed uniformly in the polymer matrix. Under the condition of uniform distribution of nanoparticles and if the size of such nanocrystals is small (2-5 nm), they don't distort an incident light wave and the light scattering is low. If to use high refractive index nanoparticles such as ZnS, CdS, ZnO, TiO2 incorporation of nanoparticles into polymer will result on significant increasing of refractive index of material. Same time these material has a proprieties of homogenous semiconductor material because of small nanometer size distance between semiconductor nanoparticles and easy tunnel transportation of charge carrier. Nanocomposite with high concentration of small size nanocrystals becomes effectively a homogeneous medium, having semiconductor proprieties of inorganic material with low scattering and good flexibility and processability of polymer. The set of properties of this mixture is determined by both components, namely polymer and nanocrystals, and

by the ratio of concentrations of them. The main efforts of research directed to develop quasi- homogenous nanocomposite material with nanoparticles and polymer matrix comparable content for photonics application areas: photoresist for nanolithography, microoptics, organic solar cell and OLED.

2. Crystalline lattice of small nanoparticles

Physics of semiconductor theory use macroscopic charge carrier statistic parameters of bulk crystals for all structures types including microns and sub- microns elements in microchips. It is correct approximation now as the sizes of microchips elements more than 100 nm are more time larger in comparison to interatomic distances. In contrary, typical nanoparticles, for example CdS or ZnS with the size of 1 - 3 nm include a few atomic layers and its interatomic distance can differ essentially from same of bulk crystals. Now are a few of works where these effects are investigated.

Indeed, if to shrink elements down to the nanometer scale, creating nanodots, nanoparticles, nanorods and nanotubes a few tens of atoms across, they've found weird and puzzling behaviors unexpected for bulk and micron sized material.
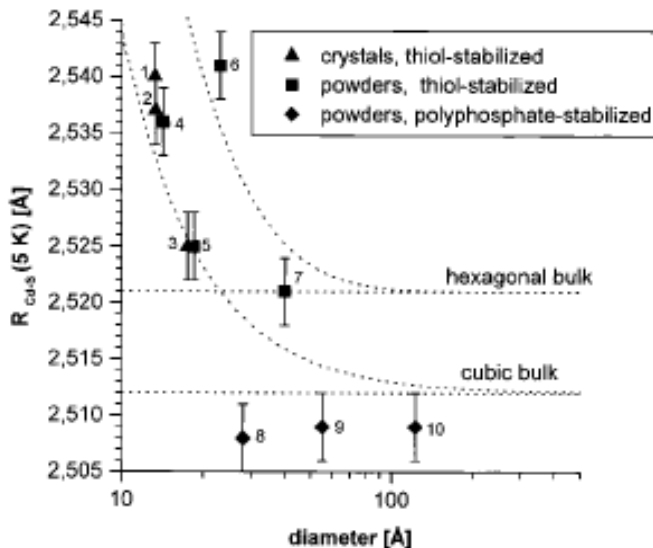

Fig. 1. Mean Cd-S distances RCd-S as a function of the size of CdS nanocrystals deduced from EXAFS experiments. Bulk values of the cubic and the hexagonal phase of CdS are also indicated (dotted).

Certainly at decreasing of nanoparticles sized up to few nanometers that correspond to some tens atoms its crystalline lattice change essentially from same of bulk crystal and it is appear instability of crystalline lattice. Large surface of small particle will result on augmentation of influence of surface states on crystalline lattice of nanoparticles.

There are a lot of work that show size and surface effects of crystalline lattice change in nanometers size nanoparticles.

In the work [1] it is shown nanoparticles crystalline lattice parameter dependence from organic substance settled on its surface and its size. Micron size particles, for example CdS have crystalline lattice similar to bulk crystals at decreasing of nanoparticles sizes down to nanometers range its lattice change essentially.

In Fig. 1 show Cd-S distance dependence from nanoparticles diameter and organic shell nature.

A few CdS samples have been investigated, the particles differing in size and crystal structure:

- three samples of polyphosphate-stabilized nanoparticles with cubic crystal structure (diameters approximately 3.0-12.0 nm),

- four samples of thioglycerol-stabilized particles (hexagonal and cubic (see below), diameters from 1.4 to 4.0 nm), and

- three samples of crystallized nanoparticles, the structures and superstructures of which are known from SC-XRD (diameters from 1.3 to 1.7 nm).

Microcrystalline CdS of hexagonal crystal structure was used as a reference substance. The smallest "particles" investigated consist of a three-dimensional network of $Cd_8(SR)_{16}$ units (R) thioglycerol), which may serve as a model for the surface of thiol-stabilized CdS nanocrystals. The other two crystallized clusters ($Cd_{17}S_4(SR)_{26}$ and $Cd_{32}S_{14}(SR)_{36}$, R) mercaptoethanol and 1-mercapto-2-propanol, respectively) may be regarded as fragments of the cubic (zinc blende) phase of CdS and appear tetrahedrally. Thus, at least for the latter three samples, "diameter" is to be taken only as a reference point for the "size" of the particles. EXAFS spectra have been taken in transmission mode at the Cd K-edge in the energy range from 26.4 to 29.0 kV at temperatures between 5 and 296 K.

All of the samples clearly showed the Cd-S coordination shell, whereas the Cd-Cd coordination (second shell) was visible in particles larger than 3.0 nm only. Figure 1 shows the dependence of the Cd-S bond length as a function of the particle diameter deduced from the EXAFS analysis. The quality of the data allows us to divide the plot into three regions. Samples 8-10 exhibit a slight contraction of the Cd-S bond with decreasing particle size, which is due to the minimization of the surface energy, obviously unhindered by the ionically bound stabilizers.

In contrast, the covalently bound stabilizers of samples 1-5 expand the Cd-S bond. This expansion is larger for the smaller particles, and it becomes larger as the steric interaction among the stabilizers comes into effect. For samples 1-3, the bond lengths determined by EXAFS match very well those from the SC-XRD analysis. From P-XRD, sample 7 is assigned to the hexagonal crystal phase, by means of which the larger mean bond length, compared to samples 8 and 9 (similar size but cubic phase), is explainable. Like sample 7, sample 6 is prepared at elevated temperatures, which makes it likely that this sample also belongs to the thermodynamically stable hexagonal crystal phase (P-XRD does not allow an unambiguous assignment). This guess is corroborated by the "out of order" bond length (Fig. 1) and by the analysis of the third moments of the pair distribution function (Fig. 1). According to the surface-to-volume ratio of the nanocrystals, this quantity increases with decreasing particle size but is divided into two groups: on one hand, all particles clearly belonging to the cubic structure (four equivalent Cd-S bonds lead to $C3$) for the largest particles) and on the other hand, samples 6 and 7, with distinctly elevated anharmonicity (in hexagonal CdS, three Cd-S bonds are equivalent, and one differs from those). Thus, for sample 6, we are in a position

to state the assingnment to the hexagonal phase by means of EXAFS spectroscopy, which has not previously been possible, by applying P-XRD and HRTEM. The Debye temperatures and static disorders are extractable from the EXAFS data together with the bond lengths and anharmonicities, as mentioned above. The Debye temperatures that were determined increased slightly with decreasing particle size, which points to a stiffening of the Cd-S bonds. When compared to the bulk value, all of the nanoparticles displayed an elevated static disorder, which, in the first instance, increases with decreasing size according to the surface-to-volume ratio (samples 10-6). For the very small clusters of samples 1-5, again slightly reduced static disorders are observed (in good agreement with the SC-XRD of samples 1-3). Possibly, this finding is a hint toward different regimes of particle growth: thermodynamically controlled growth leads to a crystallizable species, whereas subsequent Ostwald ripening yields larger and less specific colloids.

At decreasing of nanoparticles sizes up to 1 nanometers distances in crystalline lattice between metal atoms will increase that result of moving from crystalline to amorphous state of material in result. Transformation from crystalline to amorphous form of small particles well known for Fe_2O_3, Se, inorganic materials.

3. Methods of preparation and stabilization of semiconductor nanoparticles

3.1 Inorganic nanoparticles based nanocomposit

From 90 years was develop the main methods of nanoparticles synthesis. Few nanoparticles types now is commercial available from Aldrich and other commercial supplier. Methods of the nanoparticles synthesis can be divided into three main groups.

1. Synthesis of semiconductor nanoparticles in solutions of the corresponding salts by controlled addition of anions (or cations) or by hydrolysis [2];

2. Preparation of nanoparticles as a result of phase transformations [3];

3. The synthesis of nanoparticles in aerosols [4].

Preparation of nanocomposite material having both high nanoparticles concentration, absence of its coagulation and homogeneous optical and semiconductor proprieties is a mostly difficult problem. Usually it accomplished by preparation of suitable nanoparticles with modified surface and then to its incorporation in polymer, having surface active proprieties often.

For consideration of nanoparticles state in nanocomposite, we should assume that nanoparticles can interact with polymer matrix with formation of ordered polymer layers in its surface. In the work [5] was made numerical study of state of nanoparticles (fullerene) in polymer matrix and received interesting results on this bi- phase system elastic proprieties.

The purpose of this work is to investigate the effect of nanoparticle size on elastic properties of polymeric nanocomposites using MD simulations. For this, molecular models of a nanocomposite were constructed by reinforcing amorphous polyethylene (PE) matrix with nano sized buckminister fullerene bucky-ball (or simply bucky-ball). Bucky-balls of three different diameters (0.7, 1.2 and 1.7 nm, respectively) were utilized to incorporate size effect in the nanocomposites. To represent them as a generic nanoparticle system, all bucky-balls were configured as rigid body. This is necessary because a bucky-ball embedded inside the polymer matrix may deform excessively depending on its size and may overshadow the composite mechanical properties attributed to filler size. The assumption of rigid bucky-ball will ensure that the shape of filler does not contribute to variation in elastic properties. The

assumption may be unrealistic for large diameter buckyballs, it is a reasonable assumption for small bucky-balls and solid nanoparticles. In addition to this shape constraint, the volume fraction of the filler, matrix characteristics (density, molecular weight, molecular weight distribution, branch content, degree of crystallinity, etc.) and their force interaction with the nanoparticle were kept constant in all nanocomposites. Molecular models of the neat PE matrix were also developed for comparison. Elastic properties of the neat and nanocomposite systems were then evaluated using four different modes of deformation, namely, unidirectional tension and compression, and hydrostatic tension and compression, respectively.

Molecular models of nanocomposites were developed by symmetrically placing a spherical fullerene bucky-ball in the PE matrix, as shown schematically in Fig. 2. The dashed box in Figs. 2 a and b indicates the periodic cell or unit cell that was simulated by MD. Three types of bucky-balls, C60, C180 and C320 (subscripts denote number of carbon atoms), were used to incorporate the size effect. All bucky-balls were infused in matrix by approximately 4.5 vol%. Periodic boundary conditions were employed to replicate the unit cells in three dimensions. In nanocomposites, the PE matrix was represented by united atom (UA) –CH2– units. The initial structure of the matrix was constructed by positioning the bucky-ball at the center of the unit cell and by randomly generating PE chain(s) on a tetrahedron lattice surrounding the bucky-ball.
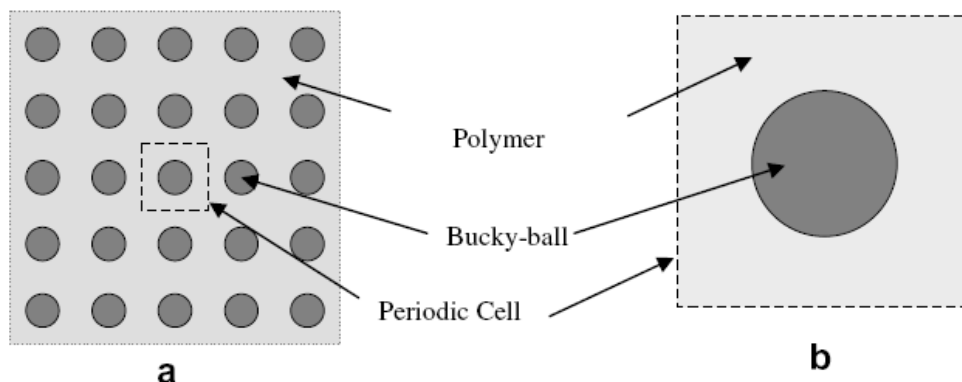

Fig. 2. (a) Schematic diagram of polymer nanocomposites, (b) periodic cells used for MD simulations.

Numerical simulation shown that elastic properties of nanocomposites are improved appreciably with the infusion of bucky-balls in PE matrix. The trend shows that with the increase in filler size, the extent of enhancement in elastic properties is gradually reduced. The result is somewhat surprising because in all cases the volume fraction was maintained constant (4.5%).

It can be concluded from this observation that size of the filler has considerable influence on polymer density even with non-bonded inter-molecular interactions between polymer and nanoparticle. The effect can be well understood from the radial density distribution of PE for both neat and nanocomposites, as shown in Fig. 3 in which the distribution is constructed by measuring local densities of PE at various radial distances starting from the center to the

half-length of the periodic box. It is interesting to find that local densities are not constant along the radial distance. A 200–250% increase in polymer density exists for all nanocomposites at a distance close to the nanoparticle. At further distances, the distribution fluctuates in a similar manner as in the neat polymer system. The fluctuating character is inherent because mass needs to be conserved [6]. The collective contributions of these factors yielded a decreasing trend in polymer bulk density with the increment of filler size. It appears from the analysis that polymer density distribution plays the foremost role in size effect. However, it is not elucidated why size difference influence polymer density. The discernible contribution from filler size can be realized from radial distribution plot as shown in Fig. 4.
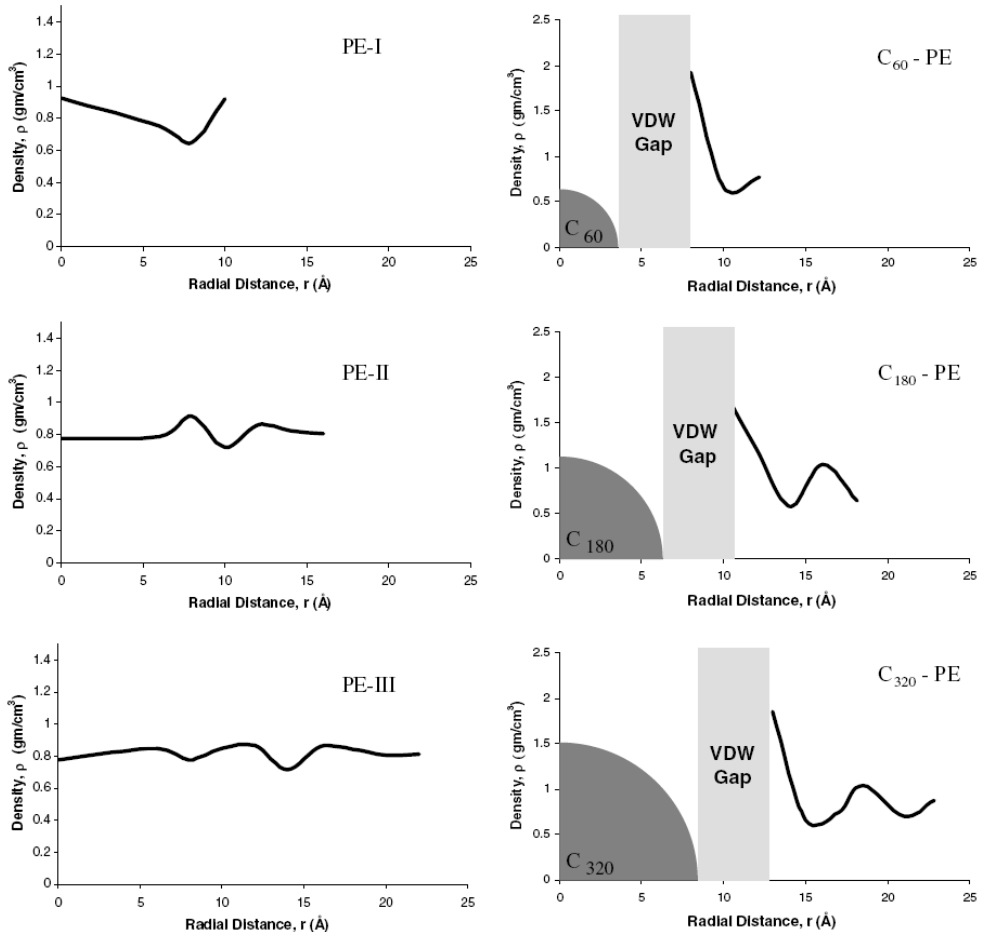
Fig. 3. Radial density distribution of various: (a) neat PE and (b) nanocomposite models. Space occupied by nanoparticles is schematically shown by the quarter circles.
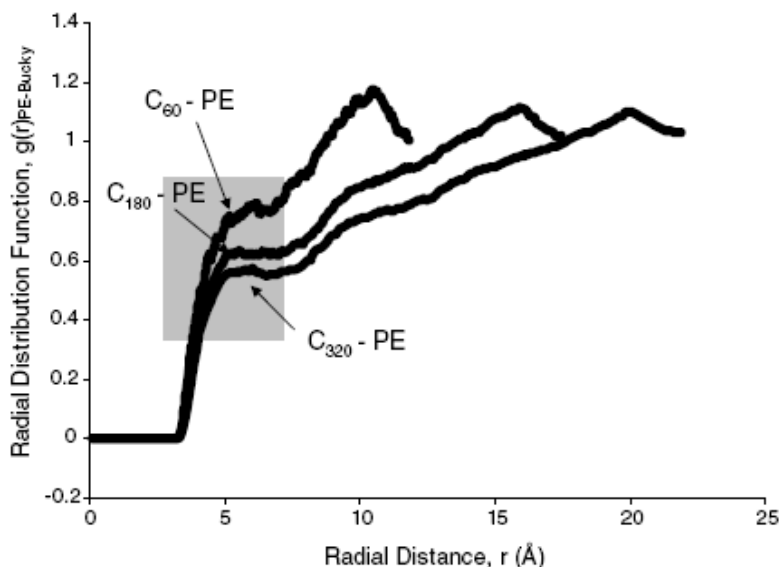
Fig. 4. PE-Bucky radial distribution functions (RDF) of various nanocomposite models.

It is known that the radial distribution function for any atom pairs gives a measure on how corresponding atoms are distributed in three-dimensional space due to VDW interactions. Hence, g(r)PE-Bucky refers to radial distribution of PE atoms with respect to Bucky-ball atoms. As atomic position of all bucky-balls were fixed, a plot of g(r)PE-Bucky would thus provide information about the polymer distribution due to interaction with a nanoparticle. Fig. 4 reveals that the size of Bucky-ball has strong influence on the g(r) plot. It is observed that the value of g(r) assumed zero from 0 to 3.4 A ˚ for all nanocomposites, then increases with radial distance. The zero value refers to the VDW thickness h. It is also evident that *h* does not depend on filler size. It is quite expected because parameters describing LJ potentials are identical for all nanocomposites and the nature of the h is known to be governed by such interactions between nanoparticle and polymer [7]. However, the relative distribution of polymer atoms towards the nanoparticle, as indicated by the variation in g(r) at a particular radial distance, is quite different with the change in filler size. It is obvious from Fig. 4 that more atoms are tending to disseminate across the polymer–nanoparticle interface as the size of buckyball decreases.

It appears from the above discussion that with the reduction in filler size, the bulk density of polymer and the attractive interaction energy between polymer and nanoparticle at the interface increase substantially. Enhancements of these parameters are then translated to improved elastic moduli.

Preparation of nanocomposite with high nanoparticles content.
According to above numerical simulation and discussion there are strong interaction between polymer and nanoparticles. At rapprochement of nanoparticles up to distance of 3 – 5 nm nanocomposite behavior change dramatically. In real nanocomposite with nanoparticles size of 2-3 nm these condition of nanoparticles – nanoparticle distance about 3 nm begin with about 10 vol. % nanoparticles concentration. So, 10 % is a border between

usual nanocomposite with no nanoparticles interaction and high nanoparticles concentration composite where nanoparticle – nanoparticle interaction play the main role in behavior formation of whole composition.

At preparation of nanocomposite with high nanoparticles concentration a contradiction is appear: to avoid nanoparticles coagulation we need to increase interaction between them and the polymer matrix, but at the same time those interactions with polymer will result in hardening of the composites in result of polymer cross-linking over nanoparticles.

In most part research this contradiction has been avoided by use of very fast drying of material [8]. At fast drying nanoparticles have not enough time for coagulation and solid material keep good distribution take place in solution. In that works, the dangerous stage of particles interactions passed fast and the composites kept their transparency. For example, if a layer is prepared by spin coating, the process of solid coating preparation occupies only some part of a second. Certainly, this method is not suitable for preparing thick nanocomposite layers and bulk nanocomposites.

Next two works show possibility to obtain high nanoparticles concentration in material that suitable to obtain high refractive index homogenous nanocomposite material based on high concentration of ZnS or CdS semiconductor nanocrystals in polymeric matrix. Same homogenous nanocomposite with high semiconductor nanoparticles concentration around 20 - 30 vol % are suitable as a homogenous semiconductor materials, so synthesis of these materials were described in detail here.

One example of high concentration ZnS nanocomposit thin film preparation give the work [8].

In the work was used previously prepared ZnS-monomers prepolymer that was UV-cured at once after spin coating in thin film. UV curing technology was used to rapidly prepolymerize the ZnS–macromer system, and then a radical polymerization process was carried out to complete the polymerization reaction. Another advantage of using this macromer is that the macromer in solution has a viscosity, which is favorable for spin-coating to form films. Furthermore, a polymerizable moiety as capping agent has also been utilized to modify the surface of ZnS nanoparticles in order to immobilize the ZnS particles into the polymer. Research on the preparation of nanoparticles–polymer composites using polymerizable surfactants, ligands or capping agents has previously been reported [9, 10]. This approach can effectively avoid the phase separation and results in transparent composites because the functionalized inorganic particles with polymerizable vinyl groups can be copolymerized with the monomers to form integrated polymeric materials.

In this work firstly was being synthesized the thiophenol (PhSH)–4-thiomethyl styrene (TMSt)-capped ZnS nanoparticles with high concentration in DMF. Then a UV curable urethane-methacrylate macromer (UMM) was introduced into the nano-ZnS containing DMF solution. The ZnS nanoparticles were immobilized into the polymer matrix via copolymerization of the macromer (UMM) with 4-thiomethyl styrene (TMSt) bound on the surface of ZnS particles to synthesize a series of nano-ZnS–poly(urethane-methacrylate macromer) (PUMM) transparent composite films with high refractive indices. The structure and composition of the thiolcapped ZnS nanoparticles were characterized via TEM, X-ray, FTIR and chemical analyses. The thermal properties, optical properties and microstructure of the nanocomposite films were investigated in detail.

Detailed description of high concentration nanocomposite synthesis method according to work [8].

3.2 Materials

Anhydrous zinc acetate, N,N-dimethylformamide (DMF), thiophenol (PhSH), thiourea, 2,4-tolylene diisocyanate (TDI), dibutyltin dilaurate (DBTL), 2-hydroxyethyl methacrylate (HEMA) and other chemical reagents were of analytical grade and were used without further purification. 4-Vinylbenzyl chloride (w 95% GC grade, Fluka) and 2,2-dimethyl-2-hydroxyacetophenone (Darocur 1173 from Ciba Special Chemicals) were used as received. 2,2′-Dimercaptoethyl sulfide (MES) was synthesized as reported previously [11]. Synthesis of 4-thiomethyl styrene (TMSt) TMSt was synthesized from 4-vinylbenzyl chloride in a manner similar to that reported in the literature [12]. 15.3 g of 4-vinylbenzyl chloride (0.1 mol), 9.12 g of thiourea (0.12 mol), 200 ml of ethanol and 0.08 g of p-methoxyphenol as inhibitor were put into a four-necked flask fitted with a reflux condenser. The reaction mixture was stirred at reflux temperature for 4 h under N_2 flow and then was cooled. 75 ml of 20% solution of sodium hydroxide were added to the above mixture, and the resulting solution was immediately heated to 80 C and continuously stirred at 80 C for 0.5 h. Finally, the resulting solution was cooled to room temperature and 100 ml of $CHCl_3$ were added. The organic phase was separated out and washed with distilled water until neutral. Then the organic phase was dried over anhydrous Na_2SO_4 and the product (TMSt) was obtained by removing the organic solvent under reduced pressure. Yield 75%, n_{20} d ~ 1.625.

The method for preparing thiol-capped ZnS nanoparticles (TCZnS) was similar to that reported in ref. [8].

3.3 Preparation of ZnS–PUMM nanocomposite films

UV curable macromers (UMM)–DMF solution of desired weight ratio, containing 2 wt% of Darocur1173 and 0.5 wt% of AIBN as initiator were mixed with 3 ml of thiol-capped colloidal ZnS–DMF solution according to the required doping content of ZnS particles in the films. The mixture solutions were concentrated to a suitable viscosity at room temperature under vacuum, and the resulting viscous solution was spincoated on silicon wafers or quartz plates at 1000–3000 rpm.

The coated films were dried under vacuum for 10 min at 45 uC, and then were exposed to the UV radiation of a medium pressure mercury lamp of 2 kW for 3 min. After UV curing reaction, the films were cured at 70 uC for 2 h, 100 uC for 1 h, 120 uC for 1 h and treated at 160 uC for 0.5 h.
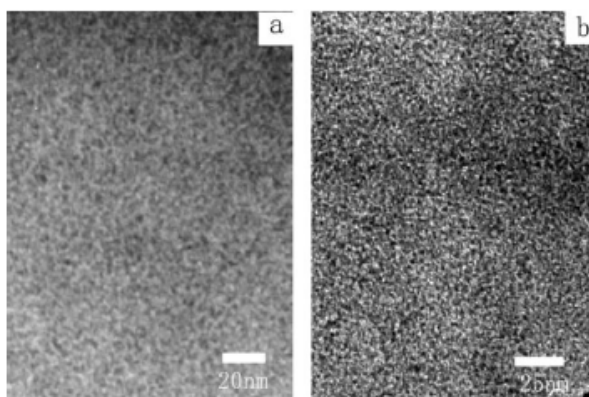

Fig. 5. TEM micrographs of the nanocomposite films of (a) TCZnS32 and (b) TCZnS79.

Resulting TEM micrographs of the nanocomposite films TCZnS32 and TCZnS79 are show in Fig. 5. The ZnS nanoparticles ranging from 2 to 5 nm are uniformly dispersed inside the polymer matrix and the ZnS nanoparticles remain their original size without aggregation after immobilization into the polymer matrix, indicating that the thiol capping agents and polymer play an important role in stabilizing and dispersing nanoparticles.

The main proprieties of nanocomposites with different content of ZnS nanoparticles show in Table 1.

The WXRD pattern of ZnS nanoparticles synthesized in the work shows broad peaks typical of samples in the nanosize regime (Fig. 6). The peaks in the diffraction pattern appearing at 2h values of 28.5, 47.5 and 56.3u correspond to (111), (220) and (311) planes of the cubic structure of sphalerite ZnS. The resulting ZnS crystallite structure is in accordance with that reported previously.
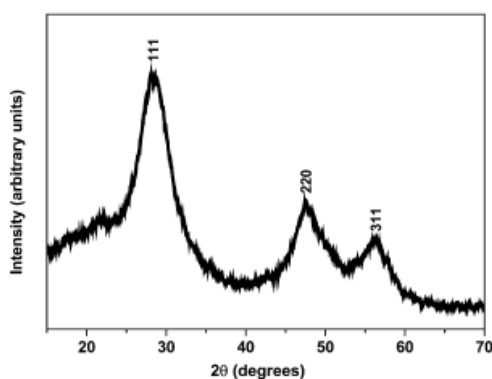

Fig. 6. Wide-angle X-ray diffraction pattern of PhSH–TMSt-capped ZnS nanoparticles.

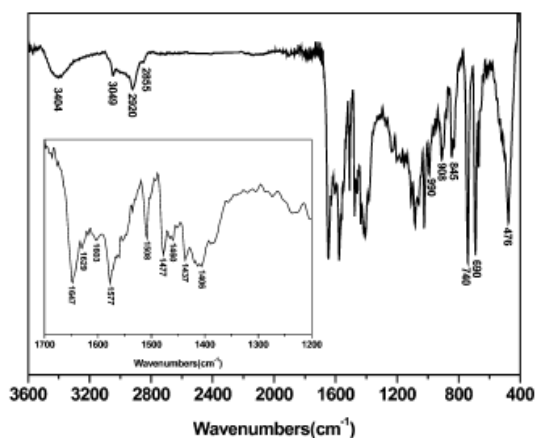The FTIR spectrum of the PhSH–TMSt-capped ZnS nanoparticles is shown in Fig. 7.

Fig. 7. FTIR spectrum of PhSH–TMSt-capped ZnS nanoparticle powder, dried from colloidal ZnS–DMF solution in vacuum.

The peaks at 2920, 2855 and 1406–1477 cm^{-1} are assigned to the characteristic vibration of the methylene groups in TMSt. The peaks assigned to C–C vibrations of benzene rings are observed at 1603, 1577, 1508 and 690–990 cm [-1]. The stretching vibration band of vinyl groups on TMSt located at 1629 cm [-1] also appears in Fig. 7 (insert), although its intensity is very weak. The absorption peak of the S–H vibration at 2550–2565 cm [-1] is not observed in the IR spectrum, indicating that the mercapto groups of TMSt and PhSH molecules were bound to the ZnS nanoparticle surface. The band of the CLO stretching vibration on residual DMF molecules is also observed at 1647 cm [-1] which is lower than that of free DMF molecules at 1667 cm [-1]. This shift reflects that there is a relatively strong interaction between DMF molecules and the surface of colloidal ZnS nanoparticles.[28] In addition, the broad peak near 3404 cm [-1] in the IR spectrum may be from the absorption of traces of moisture or adsorbed water associated with DMF.

The chemical composition of the thiol-capped ZnS nanoparticles was determined by EA and ICP-AES analyses. Anal. Found: C, 30.5; H, 2.66; S, 25.30; Zn, 42.90. The relative molar ratio of S to Zn was calculated to be 1.2 on the basis of the above quantitative analyses. This result is in good accordance with the EDAX result for ZnS particles, which showed that the ratio of the number of S to that of Zn is 1.18 within an accuracy of 2%. If all of the capping agents (RSH) are capped on the ZnS particles, the molar ratio of Zn^{2+} : S^{2-} : RS^- was calculated to be 1 : 0.6 : 0.6, based on the feed ratio (Zn^{2+} : RSH ~ 1 : 0.6), and the contents of carbon and hydrogen on the ZnS particles were also calculated to be 31.8 and 2.78, respectively. The contents of these two elements agree well with the results of chemical analyses (EA and ICP-AES) within experimental error. Therefore, it can be deduced that almost all of the capping agents, PhSH and TMSt, were capped to the ZnS particles and the molar ratio of Zn^{2+} : S^{2-} : RS^{-2} for the PhSH–TMSt-capped ZnS particles was determined to be 1 : 0.6 : 0.6.

3.4 Nanocomposite films

FTIR spectra of the ZnS–PUMM nanocomposite films for the TCZnS16–TCZnS79 are shown in Fig. 8 (X is weight percent of PhSH–TMSt-capped ZnS particles in the films). The absorption peaks at 3300 and 1657 cm^{-1} are attributed to N–H and CLO bonds of urethane linkages and the latter covers the characteristic peaks of CLO of methacrylate groups.
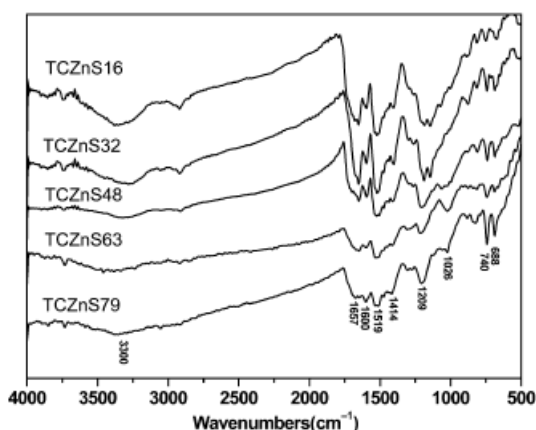

Fig. 8. FTIR spectra of nanocomposite films of TCZnS16–TCZnS79.

The CLO band gradually decreases in intensity with increasing TCZnS nanoparticles, compared with the intensity of the characteristic absorption band of phenyl (688–740 and 1600 cm-1). This result indicates that an increasing amount of TCZnS with high phenyl content is immobilized into the PUMM matrix. The IR absorbances of the CLC double bonds at 1629–1639 cm-1 for the methacrylate groups and the capping agent (TMSt) disappear, indicating that they have completely polymerized. Fig. 9 illustrates TGA curves of pure PUMM, TCZnS16, TCZnS48 and TCZnS86 films at a heating rate of 10 °C min-1 under nitrogen atmosphere from 50 to 750 °C.
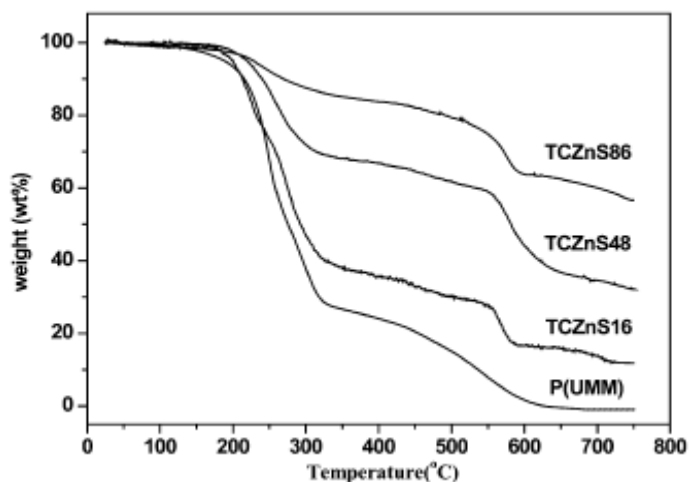

Fig. 9. TGA curves of nanocomposite films of TCZnS16, TCZnS48 and TCZnS86 at a heating rate of 10 oC min-1 under nitrogen flow.

The nanocomposite films have the initial decomposition temperatures of 201, 204 and 203 °C for TCZnS16, TCZnS48 and TCZnS86 respectively, and these values relate to the decomposition temperature of the polymer matrix (PUMM). There are two obvious weight loss regions: between 200 and 330 °C, and from 550 to 600 °C. The weight loss between 200 and 330 °C is predominantly attributed to the weight loss of the polymer matrix. The secondary weight loss at 550–600 °C is considered to be the weight loss of another part of the polymer and the thermal decay of the partial thiol-capped agents on the surface of ZnS nanoparticles. As shown in Table 1, the residues of the nanocomposite films TCZnS16–86 at 750 °C are in the range of 11.5–56.5% and they increase with increasing TCZnS content in the films. By and large, these char yields are in agreement with the theoretical weight fraction of inorganic ZnS contained in the films, indicating that the ZnS particles were successfully incorporated into the polymer matrices. This result also effectively supports the chemical analysis results for the TCZnS particles. Fig. 10 shows DSC curves of PUMM, TCZnS16, TCZnS48 and TCZnS79 films at a heating rate of 10 oC min-1 under nitrogen flow.
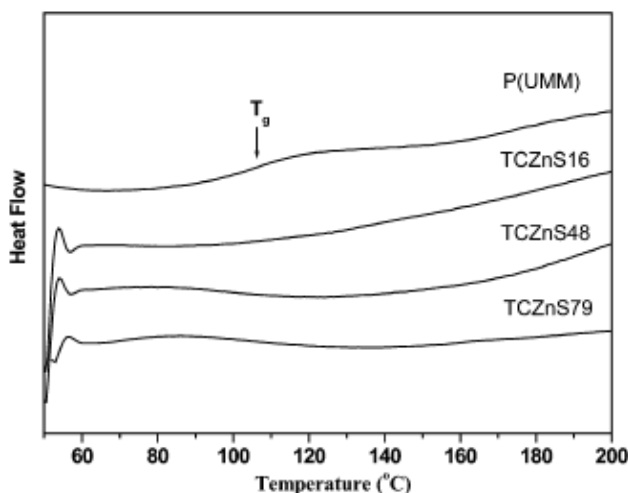
Fig. 10. DSC curves of PUMM, TCZnS16, TCZnS48 and TCZnS79 films at a heating rate of 10 oC min-1 under nitrogen flow.

The pure PUMM polymer exhibits a glass transition temperature (Tg) of about 106 oC. However, no significant thermal transition peaks are observed for the ZnS–PUMM nanocomposites below 200 oC. Also was used the torsion braid analysis (TBA) to measure the thermal transition behavior of the nanocomposite samples. The Tg of the polymers still are not observed. This suggests that nanocomposites have higher rigidity and crosslinking density due to the incorporation of the thiol-capped ZnS nanoparticles, which restricted the motion of the polymer chain segments. Thus, it may be that the glass transition temperature of the polymer is close to the decomposition temperature of it. Thermal analyses indicate that the ZnS nanoparticles were successfully immobilized into the polymer matrix and the nanocomposite films exhibit a good thermal stability.

Maximal weight concentration of thiol capped ZnS is around 86% as at higher concentration nanocomposite films with good mechanical properties cannot be obtained.

Another example of ZnS and CdS high concentration nanocomposite give the work [13, 14].

In the work has involved nanoparticles stabilization primarily by steric barriers. So, each nanoparticle should be covered by quite a thick shell linked with the surface of nanoparticle. This was accomplished by having a multi-atom chain connecting the acid group and aromatic group of the shell molecule.

Was used UV curable monomers with an acid group at one end and a vinyl group at the other and low viscosity at room temperature to accomplish both bonding to nanoparticle surface and, same time, possibility to UV-curing. Based on these requirements one suitable substance has been chosen: 2-carboxyethyl acrylate (CEA). This substance has an acrylic group for curing and can be used as shell material because of the acid group. This molecule has only a short distance between the groups, and only a relatively thin shell would be expected before polymerization. And we know that a thin shell formed at synthesis of nanoparticles is not enough at high nanoparticles concentration in a thermoplastic matrix. Certainly, we would expect additional monomer units to add to the shell monomers during the UV curing reaction.

The method to introduce the ZnS nanoparticles into CEA found is the following: ZnS nanoparticles with the shell of 5-Phenylvaleric acid have been put into toluene and heated for 10 hours at 80 °C. This operation is needed to remove residue water from the nanoparticles surface. After the nanoparticles powder was dried in air at 80 °C during 10 minutes, it was put into CEA. Ultrasonic dispersion for about 30 – 40 minutes in apparatus was done.

After dissolution of ZnS into CEA, a shell of CEA is formed at the surface of each nanoparticle. As the result ZnS – CEA nanocomposite dispersion (or solution) is stable for a long time.

UV curing of nanocomposite was made by usual way by addition of photoinitiator and curing a film with UV light. Experimental conditions: photoinitiator Dimethoxy phenyl acetophenone 0,1 w%, film thickness 100 um, UV light 365 nm, 5 mW/cm², room temperature, time of curing 10 minutes. Maximal ZnS volumetric concentration in the compositions was 25%. The resulting RI of the UV cured film was 1,65, compared with an RI of 1,45 for the pure CEA film. Thus, the RI increase is 0,20. Dependence of RI on nanoparticles concentration is shown in Fig. 11 Maximal nanoparticles concentration has been limited by viscosity increase up to the point of a non-flowing composition.
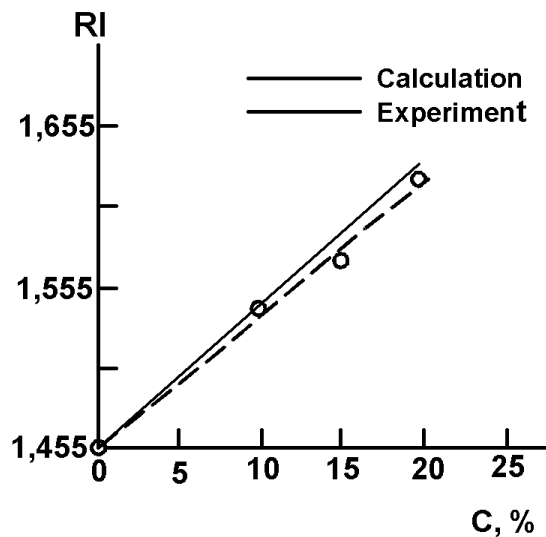

Fig. 11. Dependence of nanocomposite RI on nanoparticles concentration.

TEM photo (Fig 12) shows inside structure of nanocomposite. The photo was made of a nanocomposite cured immediately after preparation. The nanoparticles concentration is 20 vol.%. Note that the distribution of particles is almost uniform, which explains the transparency.
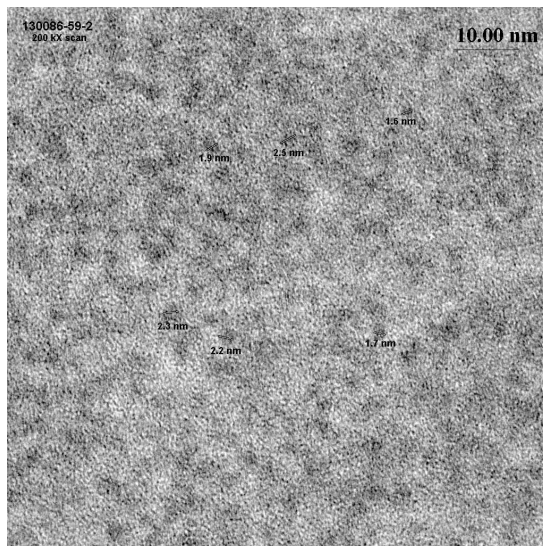
Fig. 12. TEM photo of ZnS-CEA nanocomposite (nanoparticles concentration is 20 vol. %)

4. Electron and hole transport over disperse nanocomposite systems and nanolayers

At present time charge transport over disperse semiconductor were investigated mostly for organic conjugated materials. For high concentration nanocomposite materials are used same understanding. In this chapter will be considered charge transport over disperse organic materials as the nearest analog of nanocomposite.

At organic materials when atoms are bonded together to form a molecule, the upper atomic orbitals interact with each other to form delocalized molecular orbitals while the deep atomic orbitals are still localized in the atomic potential well (Fig. 13 a) [15].
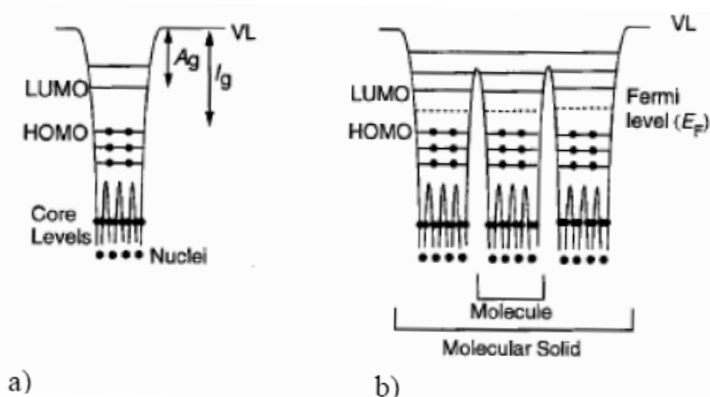

Fig. 13. Electronic structures of (a) a polyatomic organic molecule or a single chain polymer and (b) an organic solid.

When the orbital overlap occurs directly between the nuclei of the atoms, the orbitals form σ-bond and the sideway overlapping of the orbitals form π-bonds. Materials having π-bonds orbitals are named as conjugated materials same time. It is the π electrons which mainly determine the electronic and optical properties of the molecule. In ground state, the π-electrons form the π-band and the highest energy π-electron level is known as the highest occupied molecular orbital (HOMO). In excited state, the π-electrons form the π-band and the lowest energy π-electron level is known as the lowest unoccupied molecular orbital (LUMO). The HOMO resembles the valence band and the LUMO resembles the conduction band in the inorganic semiconductor concepts. The energy separation between the HOMO and the vacuum level corresponds to the gas phase ionization energy (I_g) and that between the LUMO and the vacuum level corresponds to the gas phase electron affinity (A_g) [2.1]. In an organic solid, the molecules or polymer chains are packed closely together and result in an electronic structure as shown in Figure 13b. It can be observed that the electronic states are localized to individual molecules with narrow intermolecular band widths.

4.1 Excitons in organic

When an electron has been excited from the ground state orbital to a higher orbital, it leaves a hole in the ground state orbital. The resulting bound state of an electron and a hole due to the Coulombic interaction is called an exciton. In general, excitons can be divided into two classes. If it is delocalized with radius much larger than the interatomic spacing, it is a Mott-Wannier type of exciton. On the other hand, if it is localized and tightly bound, it is called a Frenkel exciton. In organic materials, since the excitations are often localized on either individual molecules or a few monomeric units of a polymer chain, the excitons are highly localized and are considered to be Frenkel excitons which usually have large binding energy of some tenths of an eV or even higher. For example, in the case of Alq_3, a commonly used OLED material, the exciton binding energy is ~ 1.4 eV.

4.2 Transport

According statement in beginning of this paragraph, properties of disperse systems will be considered in example of conjugated polymers charge transport theory and abbreviation of polymer semiconductor is suitable for other disperse systems included nanoparticles in polymer matrix. According to this in mostly part of recent works nanoparticles like fullerene C_{60} are investigated with large organic molecules like phthalocyanine and perylen together as component of polymeric disperse compositions.[16]

Electronic properties of polymers can be described in terms of semiconductor physics [17]. The particular framework of one dimensional periodic media is well suited to the basic understanding of an isolated polymer chain [18]. Polymers are bonded by strong covalent bonds. As π-orbitals overlap is weaker than s-orbitals overlap, the energy spacing (band gap) between bounding and antibounding molecular orbitals is larger for the $\pi–\pi*$ difference than for the $\sigma –\sigma*$ one. One can thus, in a first approach, limit the band study to the $\pi–\pi*$ molecular orbitals. Those are respectively the HOMO (for Highest Occupied Molecular Orbital) and LUMO (for Lowest Unoccupied Molecular Orbital), in terms of molecular physics. They are also the usual valance (VB) and conduction bands (CB) of

semiconductor physics, respectively σ -bonds then only contribute to the stability of the molecular structure.

In a real material also, 3-dimensional interactions play a major role in transport properties, even dominating the transport which becomes an interchain hopping process. Small molecules are bounded by weak interactions in the condensed state: Van der Waals forces. There results a weak coupling between them, the resonance integral t_1 is thus small (tenth of eV at most) [19], resulting in narrow flat bands. Mobility is thus a priori smaller in small molecules, owing to a large effective mass

$$m^* = \frac{n^2}{2}\left(\frac{\partial^2 E}{\partial k^2}\right)^{-1}$$

There can of course be exceptions to such a rule, the interdistance spacing can be small and molecular materials can in fact possess a rather large mobility. The first electrically pumped injection organic laser was indeed made from small molecules (a tetracene single crystal) [20].

Transport and mobility in organic materials require a knowledge of the charged species. A review of transport properties is given by Schott [21]. Energy levels of the charges are usually determined by cyclic voltametry for materials in solution. They can be characterized by XPS or UPS (X-ray and UV photoelectron spectroscopies) for solid materials. In small molecules, charged species are localized spatially, they are simply the cation (positive) and anion (negative) radicals. In polymers, the electron–phonon coupling leads to the so-called polarons which are charges dressed by a reorganization of the lattice [22]. Polarons may be regarded as defects in conjugated polymer chains. Such defect stabilises the charge which is thus self-trapped as a consequence of lattice deformation. So in the vast majority of organic semiconductors, transport bears all characteristics of a hopping process in which the charge (cation or anion) propagates via side to side oxidation–reduction reactions (Fig. 14.).
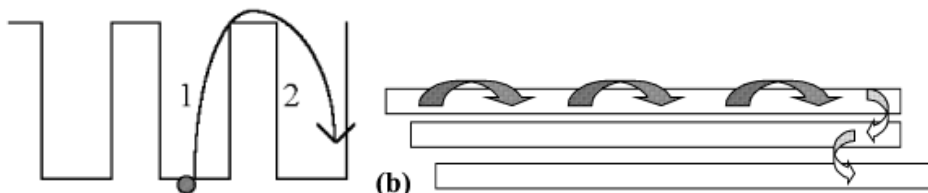

Fig. 14. Hopping process between molecules 1 and 2. b- Intra- (full arrows) and intermolecular (broken arrows) charge-transport.

One must distinguish between intramolecular charge transport along a conjugated polymer chain and intermolecular charge transport between adjacent molecules or polymer chains (Fig. 14 b.).

The former which is specific to conjugated polymers is the most efficient. Charge mobility in organics is field dependent, especially in the law mobility materials in which it usually follows phenomenologically a Poole–Frenkel law: $\mu\alpha\exp(\sqrt{E})$ [23]. Mobility can be

experimentally determined by photo-current transients (time of flight) [24], field effect transistor saturation currents [25], space charge limited currents [26] or impedance spectroscopy [27]. Mobilities in organic semiconductors are usually rather small: from 10^{-2} in well ordered conjugated polymers (liquid crystalline polyfluorene), down to 10^{-8} cm^2/(V·s) in guest–host polymer systems (dye doped poly-vinylcarbazole – PVK. Electron and hole mobilities differ by orders of magnitude in a single material; in small molecules such as the widely studied tris (8-hydroxyquinolinolato) aluminium – Alq3 – as well as in conjugated polymers such as the famous poly-paraphenylvinylene – PPV. The lowest mobilities are usually dispersive, which is the result of a distribution of mobilities [28]. Mobility can increase by up to two decades upon applying a voltage, being eventually very large above 1 MV/cm in conjugated polymers [29]. Mobility is increased by orders of magnitude when the molecular packing is improved. This is achieved by molecular ordering. Single crystals have the best performances, electron mobility in fullerene C60 single crystals is 2.1 cm^2/(V·s) [30], but it is reduced by at least 3 orders of magnitude by imperfect purification and uncontrolled crystallization [31], as well as by oxygen traps.

Charge transport is also improved by purification or deposition conditions; for instance, mobility becomes non-dispersive in Alq3 upon purification (oxygen induces traps) [32] and it becomes non-dispersive in soluble PPV derivatives upon selection of the solvent used for deposition [33]. Mobility is usually low and dispersive in randomly distributed polar molecules, but it is increased significantly when the dipoles are organized [34]. A record non dispersive electron mobility of up to $2*10^{-4}$ cm^2/(V·s) was recently achieved in an air stable amorphous glassy molecular material [35]. It is important that the mobility always drops by at least 2 orders of magnitude with impurities or defects (traps).

Light absorption and photogeneration process depend from nature of nanoparticles. If nanoparticles is inorganic semiconductor like CdS or CdSe, processes of photogeneration and absorption are similar to inorganic bulk crystals, is nanoparticles are pigment nanoparticles like phthalocyanine for example, photogeneration and absorption processes are similar to same in organic.

Charge transport over disperse system depend from concentration of charge traps in material (Fig. 11.), if concentration is low and distance between it is long, mobility become low. In nanocomposite (composition of inert polymer material and semiconductor nanoparticles) condition of charge transport over it take part at high nanoparticles concentration only. Lowest concentration limit is about 5 volumetric % of nanoparticles in material, but usually about 30 - 40 vol. % concentration is optimal for obtain charge transport over disperse nanocomposite material as over homogeneous media. Same time achievement of 30 vol. % of nanoparticles in material is a difficult task for technology.

5. Application of semiconductor nanostructures: solar cells, OLED

Important area of semiconductor nanoparticles application is n-type semiconductor layers in organic multilayer thin film structures as addition to usual p-type organic semiconductor.

Typical structure of organic solar cell as well as structure of OLED (organic light emitting device) consist organic thin layers: p-type for holes injection (OLED) or extraction (solar cell), n-type - for electrons injection or extraction in corresponding application.

5.1 Principle of operation of solar cell (PV - photo Voltaic) and OLED structures

Before discussing the development of organic PVs the basic principles are outlined. Almost all organic solar cells have a planar-layered structure, where the organic light-absorbing layer is sandwiched between two different electrodes. One of the electrodes must be (semi-) transparent, often Indium–tin-oxide (ITO), but a thin metal layer can also be used. The other electrode is very often aluminum (calcium, magnesium, gold and others are also used). Basically, the underlying principle of a light-harvesting organic PV cell (sometimes referred to as photodetecting diodes) is the reverse of the principle in light emitting diodes (LEDs) (see Fig. 15) and the development of the two are somewhat related [36].
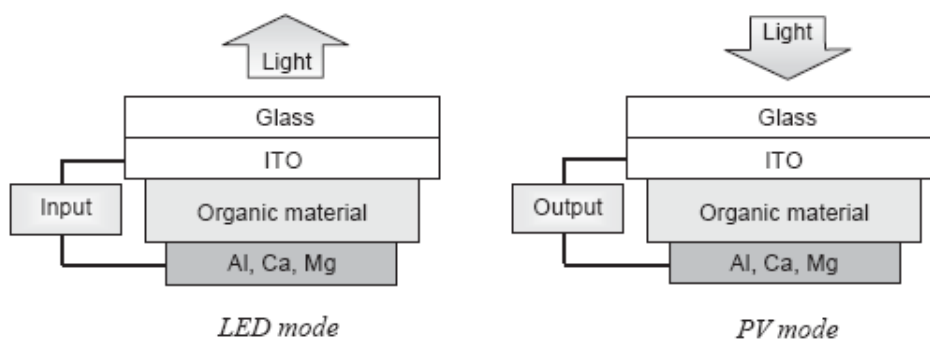
Fig. 15. A PV device (right) is the reverse of a LED (left). In both cases an organic material is sandwiched between two electrodes. Typical electrode materials are shown in the figure. In PVs electrons are collected at the metal electrode and holes are collected at the ITO electrode. The reverse happens in a LED: electrons are introduced at the metal electrode (cathode), which recombine with holes introduced at the ITO electrode (anode).
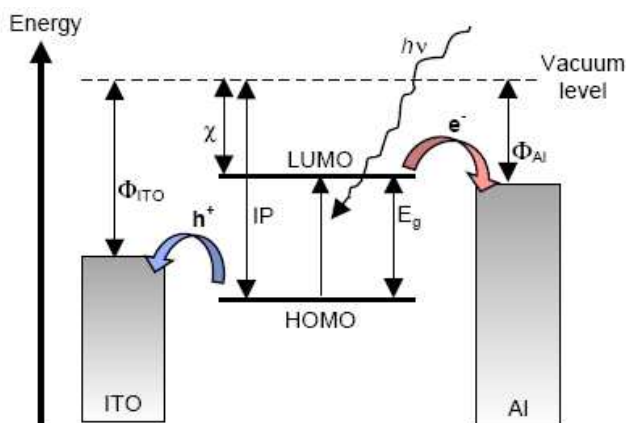
Fig. 16. Energy levels and light harvesting. Upon irradiation an electron is promoted to the LUMO leaving a hole behind in the HOMO. Electrons are collected at the Al electrode and holes at the ITO electrode. F: workfunction, c: electron affinity, IP: ionisation potential, Eg: optical bandgap.

In LEDs an electron is introduced at the low-workfunction electrode (cathode) with the balanced introduction of a hole at the high-workfunction electrode (anode). At some point the electron and the hole meets, and upon recombination light is emitted [37]. The reverse happens in a PV device. When light is absorbed an electron is promoted from the highest occupied molecular orbital (HOMO) to the lowest unoccupied molecular orbital (LUMO) forming an exciton (see Fig. 16).

In a PV device this process must be followed by exciton dissociation. The electron must then reach one electrode while the hole must reach the other electrode. In order to achieve charge separation an electrical field is needed, which is provided by the asymmetrical ionisation energy/workfunctions of the electrodes. This asymmetry is the reason why electron-flow is more favoured from the low-workfunction electrode to the high workfunction electrode (forward bias), a phenomenon referred to as rectification. The light harvesting process along with the positioning of energy levels is depicted in Fig. 16.

In the solid phase, the HOMOs and LUMOs of adjacent molecules may interact and form a conduction band (CB) and a valance band (VB) respectively (this will be described below). The shape of the CB and VB changes when the organic material is put into contact with electrodes (see Fig. 17), depending on the conductance of the polymer and on whether the electrodes are connected or not.
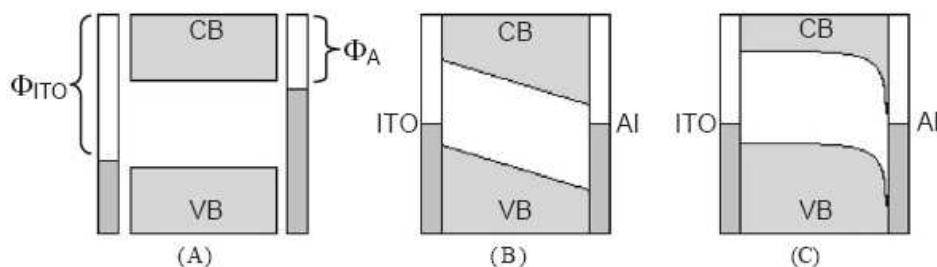

Fig. 17. The relative energy levels of the electrodes, CB and VB are shown in three situations, with no external bias. (A) CB and VB are shown along with the low-workfunction electrode (Al) and the high workfunction electrode (ITO) when isolated from each other. (B and C) The cell is assembled and short circuited, causing alignment of the electrode potentials. In (B), an insulating organic material is used. In C a hole-conducting polymer is used forming a Schottky junction at the high-workfunction electrode.

If the cell is short circuited the Fermi levels of the electrodes align (B and C), and in doing so the CB and VB are pulled skew. In B the polymer material is an insulator. This gives a field profile that changes linearly through the cell. In C a hole-conducting (p-type) semiconductor is used (most polymers are much better hole conductors than electron conductors). If the material is doped or illuminated charge carriers are generated. Due to the p-conduction properties, the generated holes are allowed to redistribute freely and they will flatten the bands approaching the high-workfunction electrode (a Schottky junction). The distance over which the CB and VB exhibit curvature is called the depletion width. In B the depletion width extends throughout the material. In C the depletion width is less than half the material thickness. Under external bias the relative electrode potentials can be changed, depending on the size and direction (forward or reverse) of the bias.

5.2 Comparison of inorganic and organic PV

In a crystalline inorganic semiconductor with a 3D crystal lattice the individual LUMOs and HOMOs form a CB and a VB throughout the material. This is fundamentally different from most organic dye semiconductors where the intermolecular forces are too weak to form 3D crystal lattices. Consequently the molecular LUMOs and HOMOs do not interact strongly enough to form a CB and VB. Thus charge transport proceeds by hopping between localised states, rather than transport within a band. This means that charge carrier mobility in organic and polymeric semiconductors are generally low compared to inorganic semiconductors. Also, charge separation is more difficult in organic semiconductors due to the low dielectric constant. In many inorganic semiconductors photon absorption produces a free electron and a hole (sometimes called charge carriers), whereas the excited electron is bound to the hole (at room temperature) in organic semiconductors. Conjugated polymers lie somewhere between the inorganic semiconductors and organic dyes. In general, excitons are considered to be localised on specific chain segments. However, there are cases where excitons seem to be delocalised. In these cases, the excitons are referred to as polarons [38, 39].

In simple PV devices and diodes based on organic semiconductors the primary exciton dissociation site is at the electrode interface (other sites include defects in the crystal lattice, absorbed oxygen or impurities) [40]. This limits the effective light harvesting thickness of the device, since excitons formed in the middle of the organic layer never reaches the electrode interface if the layer is too thick. Rather they recombine as described above. Typical exciton diffusion distances are on the order of 10 nm.

In fact inorganic PV have the best proprieties of charge carrier photogeneration and transport, polymer materials have the worst same proprieties. Organic crystalline dyes is lie between inorganic semiconductors and polymers. However flexible solar cell can be made in the basis of polymer films mostly, organic crystalline dyes can be introduced to structure as a thin layer, but inorganic semiconductors layers can not to be introduced in this structure absolutely.

From this point of view use of polymer based nanocomposite included semiconductor nanocrystals of different types (inorganic semiconductors - TiO_2, CdS; fullerenes; carbon nanotubes; organic crystalline dyes in nanocrystalline state) is the single way to combine high semiconductor proprieties of inorganic and crystalline materials with good flexibility of polymer film.

There are another advantage of inorganic semiconductor nanocrystals for PV and OLED application:

All semiconductors have a proprieties of production of single atom oxygen at presence of oxygen molecules and its illumination by light, especially in UV region. Presence of water vapor made this process more effective. Both PV and OLED device use at presence of light certainly and oxygen and water from air. Single atom oxygen produced by action of light is very reaction active chemical. Its action to thin nanometers sized polymeric structure will result on fast its destruction and degradation.

In the work [41] show results of degradation of PV structure at action of oxygen and the light. In fact presence of oxygen and the light illumination are standard conditions of PV and OLED structure application as oxygen and water vapors go easily over polymer film of flexible structure.

Fig. 18 shows the degradation of the photocurrent of a plastic solar cell under $1000 W/cm^2$ illumination inside the sealed container. Already within 1 h the effect is very pronounced. It also shows how a temporary exposure of the cell to air leads to an accelerated decrease of

photoefficiency. The photocurrent seems to become inhomogeneous, suggesting selective degradation. Higher degrees of degradation around the rim of the cell could be an effect of a mechanism of lateral degradion through diffusion of oxygen or water vapor.
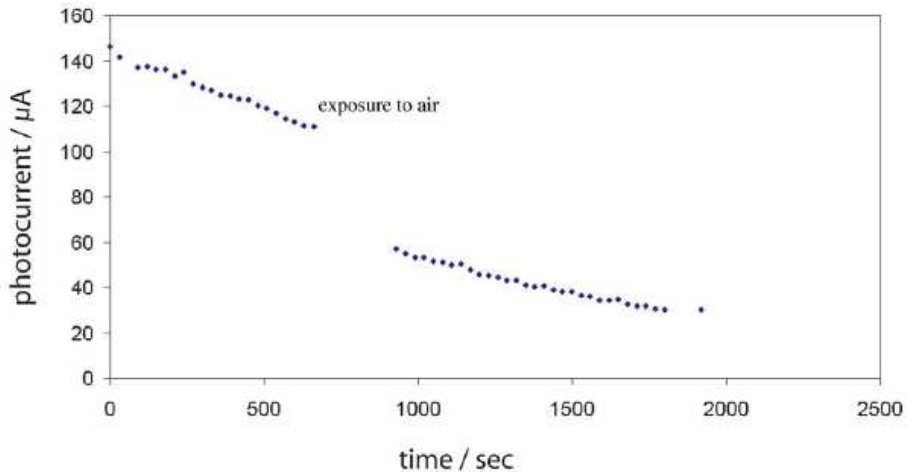

Fig. 18. Decay of photocurrent (Isc) in Cell as a result of degradation under 1000 W/cm2 illumination in an inert atmosphere, followed by exposure to the atmosphere.

From this point of view use of inorganic nanocrystals, more stable to oxygen action is preferable too.

In despite of evident advantage of inorganic and organic nanocrystals application in PV and OLED devices, practical examples are not numerous because of difficulties of thin layer preparation from new and unknown materials nanocomposites as well as because of nanocomposites preparation.

Now mostly applicable are: fullerene C_{60} nanoparticles, carbon nanowires, TiO_2 and CdS nanocrystals: all n-type semiconductors.

5.3 Example of PV structure based on fullerene

Excitons do not dissociate readily in most organic semiconductors. The idea to overcome this obstacle is use a heterojunction: to use two semiconductor materials with different electron affinities and ionisation potentials. This will favour exciton dissociation: the electron will be accepted by the material with the larger electron affinity and the hole by the material with the lower ionisation potential.

One of the most used acceptors in heterojunction cells is the fullerene C_{60} nanoparticles (or large organic molecules in some publication) [42]. Besides having a high electron affinity, C_{60} is fairly transparent and also has fair electron conductance (10^{-4} Scm^{-1}). This makes fullerenes a good component in PV cells. The first report of a conducting polymer/C_{60} cell came in 1993 by Sariciftci et al. [43]. In one study, fullerene was vacuum sublimed onto a MEH–PPV layer that was spin coated on ITO-covered glass . Au was used as the electron-collecting electrode (see Fig. 19).
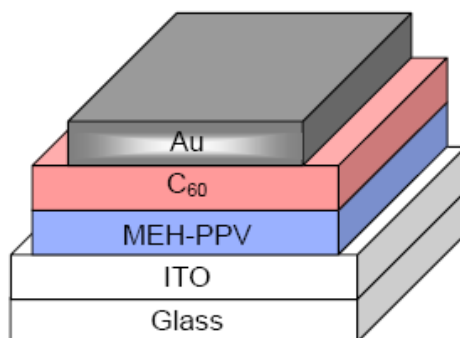
Fig. 19. A two-layer heterojunction photovoltaic cell with C60 fullerene nanoparticles. The electron accepting C_{60}-layer contacts the Au electrode, while the electron donating MEH-PPV layer contacts the ITO electrode.

In this example a defect of structure is a low light absorbing area close to border between C_{60} and MEH-PPV semiconductors. It is clear that exciton dissociation is most effective at the interface in heterojunction cells, thus the exciton should be formed within the diffusion length of the interface. Since typically diffusion lengths are in the range of 10 nm, this limits the effective light-harvesting layer. However, for most organic semiconductors the film thickness should be more than 100nm in order to absorb most of the light. It follows that thicker film layers increase light absorption but only a small fraction of the excitons will reach the interface and dissociate. This problem can be overcome by blending donor and acceptor, a concept called dispersed (or bulk) heterojunction (see Fig. 20) [41].
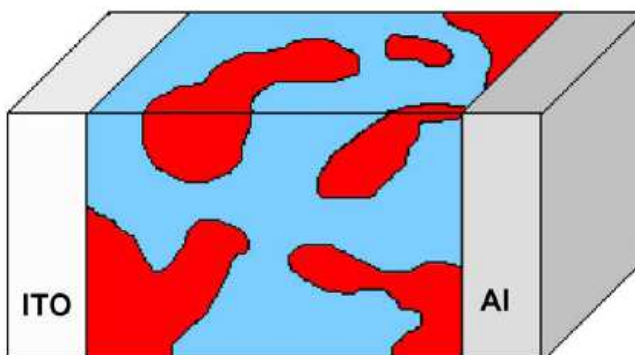

Fig. 20. Dispersed heterojunction between a transparent ITO electrode and an Al electrode.

Certainly, this structure can be prepared by mixing of polymer or polymer like materials only and use of nanocomposites here is without alternative. In 1994 Yu [44] made the first dispersed polymer heterojunction PV cell by spincoating on ITO covered glass from a solution of MEH-PPV and C_{60} in a 10:1 wt-ratio. Finally, Ca was evaporatedonto the organic layer. The cell showed a photosensitivity of 5.5 mA/W, an order of magnitude larger than the photosensitivity of the pure polymer.

One limitation of this approach is the relative low solubility of fullerenes in normal solvents. This problem was solved when Hummelen et al. [45] synthesiseda number C_{60}-derivatives with increased solubility in 1995, which allowed the fullerene content to be as high as 80% in the prepared films. Using a methano-functionalised fullerene derivative Yu et al. [46] repeated the fabrication procedure with a polymer/fullerene ratio of 20/80, the contacts were made of ITO and Ca, and the cell had a QE of 29% and a PCE of 2.9% (under monochromatic light, intensity at 20 mW/cm2). Thus a substantial increase compared to earlier polymer/fullerene mixtures. In 2000 Shaheen et al. [47] reportedhigh QE values of 85% in a PPV-derivative and fullerene heterojunction cell, with a PCE of 2.5%. All approaches described above are to use high concentrated nanocomposites based on fullerene C_{60} nanoparticles stabilized by linking to polymer chain. Different structures of fullerenes based nanocomposites materials are show in Fig. 21.

It is clear that the control of morphology in dispersed heterojunction devices is a critical point. The degree of phase separation and domain size depend on solvent choice, speed of evaporation, solubility, miscibility of the donor and acceptor etc. One strategy towards increasing control is to covalently link donor and acceptor. In 2000 Stalmach et al. [48] synthesized PPV-C_{60} diblock copolymers through controlled living radical polymerization. The same year Peeters et al. [49] synthesized a number of p-phenylene vinylene oligomers (OPV) attachedto C_{60} and investigated their use in PV devices. Peeters found that charge separation lifetimes was dependent on the number of repeating oligomer units. Thus, charge separation lifetimes were much longer for 3–4 units compared to 1–2 repeating units. A cell consisting of the longest oligomer (4 repeating units) between aluminium and a PEDOT-PSS covered ITO electrode had an ISC of 235 mA/cm² and a VOC of 650 mV, but a relatively low FF of only 0.25. Van Hal et al. [50] made a similar study on fullerene oligio (thiophene)-fullerene triads varying the number of monomer units. In agreement with Peeters they found that a certain length is needed in order to observe charge transfer upon excitation. Thus photoinduced charge transfer was much more pronounced for 6 monomer units, compared to an oligomer with 3 monomer units. Such model studies are important in understanding charge transfer and light harvesting in greater detail. In 2003 Krebs et al. [51] have made an interesting study on a dyad consisting of a poly(terphenylene cyanovinylene) terminated with an ADOTA dye. The dye is a cation and the assembly thus resembles a soap molecule and have the ability to form LB films. By spincoating the dyad on an ITO covered glass substrate, followed by evaporation of Al on the organic layer, the short circuit current of the dyad was 100 fold larger compared to the pure polymer.

While some control is introduced by covalently linking the donor and acceptor in polymer/oligomer-C60 assemblies the final morphology may suffer from phase separation and clustering of the fullerene (or dye) units, which potentially limits efficient charge separation due to low donor/acceptor interfacial area. Also, increased phase separation may disrupt the continuity of the phases and reduce the charge transport properties of the material, due to inefficient hopping between different domains, reducing overall performance. This may be a critical point, since intramolecular charge recombination might occur at a fast rate. One way to control a bicontinuous phase separation andinsure a large interfacial area between donor and acceptor is to covalently graft fullerene moieties onto the donor-polymer backbone (Fig. 21), so-called double-cable polymers (due to their p/n type conduction properties).
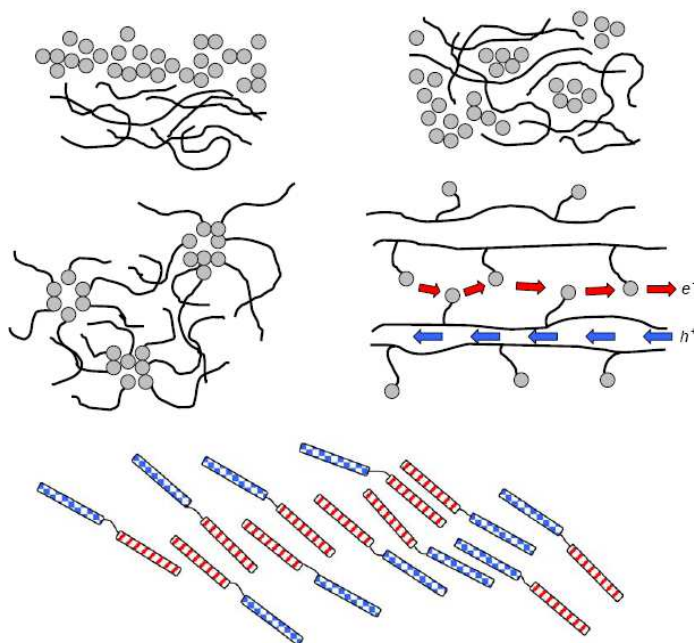
Fig. 21. Different morphologies of heterojunction cells based on fullerene nanocomposites. Top, left: Two-layered structur e of fullerenes and polymer chains. Top, right: dispersed heterojunction. Middle, left: fullerenes with polymer chains attached. Middle, right: self-assembled layered structure of double-cable polymers. Bottom: self-assembled layered structure of diblock copolymers. The layered structure of double-cable polymers and diblock copolymers are expected to facilitate efficient electron and hole transport.

These assemblies have been intensively investigated in recent years as promising components in PV devices [52], but they are also interesting as components in molecular electronics. The first reports of polymers bearing fullerene on the side chains came in 1996 by Benincori et al. [53] The polymer was a polythiophene. Cravino et al. [54] synthesiseda fullerene-thiophene double-cable and used it in a solar cell. However the PV device had limited cell efficiency due to low levels of fullerene content (C_{60} was attached to 7% of the repeating units). It is important that the fullerene content reaches the percolation threshold to insure efficient electron transport. Thus as the complexity of the designed systems increase the more critical it becomes to optimize design parameters. Even though the synthesized double cable polymers have shown some promising results, we have yet to see the fully optimized double-cable polymers. An alternative to polymer-fullerene double-cables is block copolymers consisting of a donor and acceptor block. In general block copolymers are known to phase separate and form ordered domains similar to the double-cable polymers. In 2003 Krebs et al. [55] synthesiseda block copolymer consisting of an electron acceptor block and an electron donor block. The backbone was polyacetylene, and by using phenyl and pentafluorophenyl as side groups the HOMO and LUMO of the individual blocks could be tuned so that hole or electron conductance is favored.

5.4 D well ordered bulk heterojunction based on carbon nanotubes

Dispersed heterojunction described above ensure augmentation of effective surface of junction between n and p- types of semiconductors, but same time irregular structure of n and p- types areas will result on augmentation of length of charge transportation from n and p semiconductors border to the electrodes (Fig. 20). Certainly if to make regular 3-D structure of different phases of heterojunction, it is possible to diminish charge transportation length up to thickness of the layer. This structure can to resolve problem of relative high exciton energy dissociation of organic material. Indeed, high exciton energy dissociation in organic in comparison with inorganic will result on diminish of organic solar cell efficiency (problem was described in details above of this paragraph). Same time use of polymers for flexible solar cell thin film have no alternative in classical technique as polymers materials only allow to form thin flexible film. However, if to use technique of self- assembly, it is possible to prepare polymer free thin film consist from inorganic nanoparticles and to obtain inorganic high efficiency and stable solar cell based on nanoparticles assembly structure.

 However, for practical making of these structure are need to prepare 3-D elements with tens nanometers sizes with artificial distribution of n- and p- types of semiconductor nano-sized areas that is too difficult at the present time. Now only way to make so is to use self-assembly technique for preparation of nanometers sized vertical columns from carbon nanotubes well ordered. The spaces between columns should be filled by another semiconductor. This technique will allow to produce well ordered heterojunction with charges transport distances minimized in comparison to structure in Fig. 20. At the present time investigations of self- assembly carbon nanotubes processes is in beginning only. There are a lot of both scientific and technological problems. The first practical realization of this way give a work [56]. In the fallowing text will be considered semiconductor solar cell strictures based on single carbon nanotubes and its combination with other types of nano-semiconductors: CdS nanoparticles and porphyrines organic pigments. The principle of self-assembly structure shown in Fig. 22.
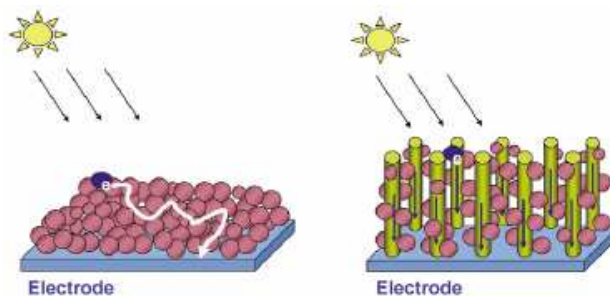

Fig. 22. Illustration of random charge carrier transport in bulk heterojunction (in the left) - charge transportation length is long and well oriented 3-D nanostructure carbon-nanotube-directed charge transport in an organized hybrid assembly.

Certainly should be take into account that each nanotubes have diameter of 1,5 nm and it is very difficult to made really this structure.

Commercially available semiconductor carbon nanotubes (SWNTs) contain both metallic and semiconducting nanotubes with different chirality. The work function of SWNT bundles is known to be about -4.8 eV versus absolute vacuum scale (AVS). Carbon nanotubes possess a bandgap in the range of 0-1.1 eV, depending upon their chirality and diameter.

Semiconducting carbon nanotubes undergo charge separation when subjected to bandgap excitation. Two different approaches can be considered for the use of carbon nanotubes in solar cells (Fig. 23):

(i) direct bandgap excitation of semiconducting nanotubes; or (ii) the use of conducting tubes as conduits to improve the transport of charge carriers from light-harvesting nanoassemblies.

The methods employed to deposit carbon nanotubes as thin films on a conducting surface for use as photoresponsive electrodes in solar cells are discussed in the following sections. Examples of the two strategies presented in Fig. 23 are also illustrated.
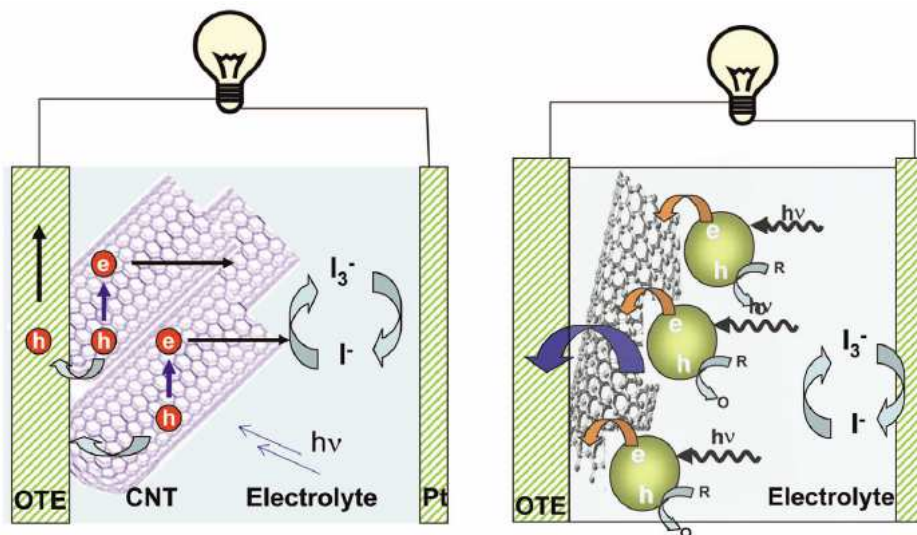

Fig. 23. Strategies to employ carbon nanotubes in photochemical solar cells: (left) by direct excitation of carbon nanotubes; (right) by excitation of light-harvesting assemblies anchored on carbon nanotubes. The electrons and holes generated by photoexcitation are referred to as e and h, respectively. One of these charge carriers is collected at the electrode surface and the other one is scavenged by the oxidized (O) or reduced (R) form of the redox couple in the electrolyte.

Photoinduced charge separation in SWNT films An interesting semiconducting property of SWNTs is their ability to respond to light. For example, the photoresponse of carbon nanotubes filaments was realized in early years from the elastic response of the aligned bundles between two metal electrodes [57]. Avouris and coworkers [58] have monitored hot carrier luminescence from ambipolar carbon nanotube field-effect transistors (FETs). The holes and electrons injected via an external circuit produce emission resulting from electron-

hole recombination in the system. The recent report of bandgap fluorescence from a semiconducting SWNT sample rich in individual nanotubes has made it possible to correlate optical properties with individual tube species as a result of their well-defined optical transitions. Spectroscopic studies have demonstrated that the relaxation of electrons and holes to the fundamental band edge occurs within 100 fs after photoexcitation of the second van Hove singularity of a specific tube structure [59]. These early studies confirm the ability of carbon nanotubes to possess a band structure that can undergo electron-hole charge separation with visible light excitation (Fig. 24).
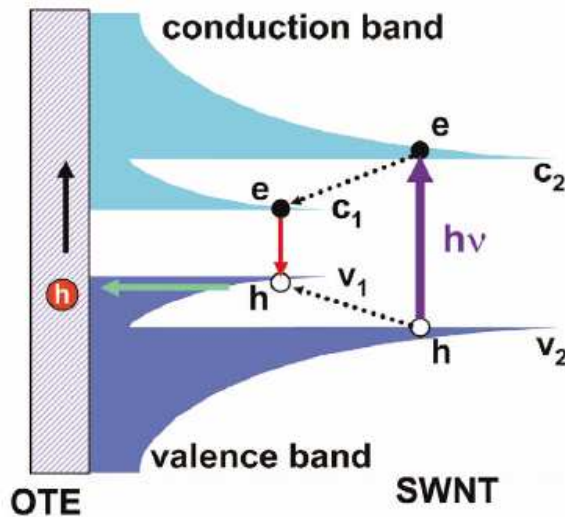

Fig. 24. Schematic illustrating the density of states of a single carbon nanotube. Photogenerated holes are captured at the collecting electrode surface, resulting in current generation in a photoelectrochemical cell. C1 and C2 refer to conduction bands and V1 and V2 refer to valence bands. e and h refer to the electron and holes generated following photoexcitation of the SWNTs.

In order to use photogenerated charge carriers for generating electricity, it is important that they are separated before undergoing recombination. However, spatially confined charge carriers in the nanotube are bound by Coulombic interactions with the bound pair referred to as an exciton [60]. Most of these excitons from higher C2 and V2 levels relax via interband transitions to the low-lying C1 and V1 levels of the fundamental gap to produce a second sub-bandgap exciton. A small fraction of the excitons are able to dissociate and form unbound electron-hole (e-h) pairs. The dissociation of excitons to create the charge-separated state thus becomes an important process to tap them into photocurrent generation. The charge separation in carbon nanotubes can be probed using femtosecond laser pump-probe spectroscopy. This technique is useful to investigate the ultrafast processes that occur following the excitation of carbon nanotubes or semiconductor materials. In a typical experiment, the absorption changes in the sample are recorded at different delay times following excitation with a short laser pulse. Difference absorption spectra at various delay times have been recorded by exciting SWNT suspensions in THF

A review of high nanoparticles concentration
composites: semiconductor and high refractive index materials
137

with a 387 nm laser pulse (pulse width 130 fs). (A Clark MXR-2010 laser system and Ultrafast Systems detection setup was used for these measurements.) Representative transient absorption spectra and the decay of absorption at 700 nm are shown in Fig. 25.
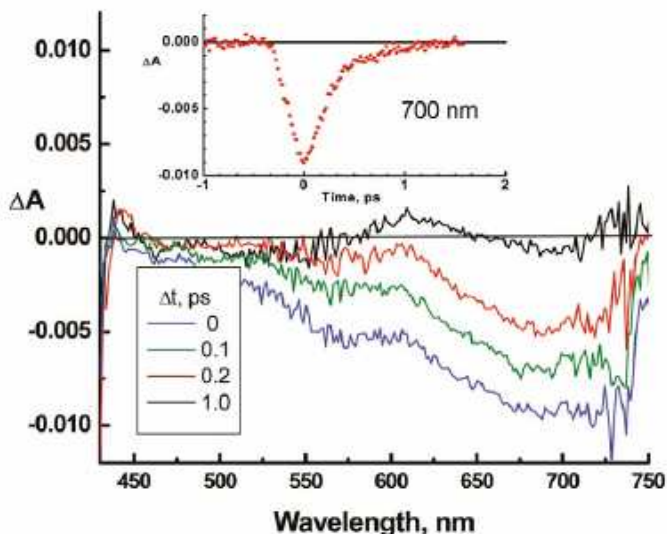

Fig. 25. Time-resolved transient absorption spectra of an SWNT suspension in THF (flow cell) recorded using a 387 nm laser pulse (pulse width 150 fs; $\Delta t = 0$ corresponds to the end of the pulse). The inset shows the bleaching recovery at 700 nm.

The photoexcitation causes the bleaching of SWNT absorption in the red region. The broadness of the bleaching band essentially arises from the diversity of tube diameters, chiral angles, and the aggregation of nanotubes.

The bleaching in the visible region, which corresponds to the C2-V2 transition, recovers in ~1 ps as the bound electron-hole pairs or excitons relax to the low-lying C1-V1 state. The dynamics of the transient bleaching recovery and the decay of the emission in the infrared arising from charge recombination in the fundamental gap have been studied recently by Ma et al. [59]. They observed that the electron-hole pairs accumulate in the fundamental gap (C1-V1) and their lifetime (10-100 ps) is dependent on the excitation intensity. Based on the difference between the emission decay and transient absorption recovery, these researchers highlighted the involvement of charge trap states as the additional contributing factors responsible for electronic transitions. The presence of such surface states are likely to stabilize the photogenerated charge carriers and contribute to the overall photocurrent generation. Such enhanced charge separation is crucial for increasing the probability of charge collection at the electrode surface. The transient bleaching observed following laser pulse excitation shows that there is a significant number of charge carriers produced in the SWNTs. The obvious question is whether one can collect the photoinduced charge carriers generated in SWNTs suitably for photocurrent generation, similar to the photovoltaic application of other semiconductors.

5.5 SWNT-semiconductor hybrids

In photoelectrochemical cells based on nanostructured or mesoscopic semiconductor films, the electron transport across particles is susceptible to recombination loss at the particle grain boundaries. The use of a nanotube support to anchor light-harvesting assemblies (e.g. semiconductor particles) provides a convenient way to capture photogenerated charges and transport them to the electrode surface. An illustration of these two scenarios can be seen in Fig. 23.

SWNTs are an ideal candidate as conduit for collecting and transporting charges across light-harvesting assemblies. Of particular interest is a CdS-SWNT composite that is capable of generating a photocurrent from visible light with unusually high efficiency [61]. The luminescence of CdS is quenched by SWNTs. Transient absorption experiments have confirmed the quick deactivation of excited CdS on a SWNT surface, as the transient bleaching recovers in about 200 ps.

In order to test the hypothesis of electron transfer between excited CdS and SWNT in the composite film, CdS particles are deposited on SWNT electrodes (referred to as OTE/SWNT/CdS) [62]. The SWNT film was first deposited on the OTE using the electrophoretic deposition method described earlier. The electrode was then sequentially immersed in solutions containing Cd^{2+} and S^{2-} to form CdS nanocrystallites. The electrode was thoroughly washed with deionized water between the two immersions so that only adsorbed Cd^{2+} ions react with S^{2-}. It may be noted that such an ion adsorption precipitation method is similar to methods employed for casting nanostructured films of metal chalcogenides on oxide films [63]. It is interesting to note that Cd^{2+} ions readily adsorb on SWNTs and react with S^{2-} to form CdS nanocrystallites with a characteristic onset absorption around 500 nm.

It is employed the OTE/SWNT/CdS electrode in a photoelectrochemical cell containing acetonitrile solution with 0.1% triethanolamine as a sacrificial electron donor. Triethanolamine undergoes irreversible oxidation as it scavenges photogenerated holes from the electrode surface. Photocurrent generation is seen when the CdS-modified SWNT film is irradiated with visible light ($\lambda > 380$ nm). An open circuit voltage of ~200 mV and a short circuit current of 6.2 µA were recorded. The dependence of the IPCE on the excitation wavelength is shown in Fig. 26.
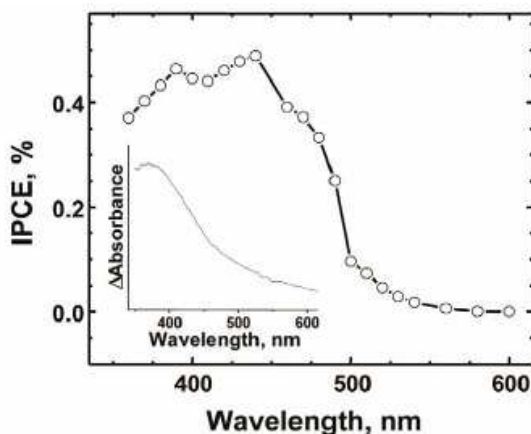

Fig. 26. IPCE of OTE/SWNT/CdS. Inset: absorbance difference between OTE/SWNT/CdS and blank SWNT film.

The onset of IPCE is seen at ~500 nm and closely follows the absorbance characteristics of CdS (see inset of Fig. 26). The observed photocurrent is dominated by the initial excitation of CdS as is evident from the photocurrent action spectrum. Furthermore, the anodic current observed with SWNT/CdS films confirms the direction of the electron flow from CdS to the collecting electrode mediated by the SWNT network. The ability of the CdS-SWNT nanocomposite system to undergo photoinduced charge separation opens up new ways to design light-harvesting assemblies.

5.6 TiO$_2$ nanoparticles based PV

In the work [64] was used TiO2 nanoporous film in structure of dye sensitized solar cell. Nanoporous film is real alternative to high concentration nanocomposite. Preparation of high concentrated homogenous nanocomposite is a difficult task as nanoparticles tend to coagulated at high concentration. Same time nanoporous film have uniform distribution of pores with its high volumetric concentration - up to 60 %. If to fill nanopores by polymer we obtain stable nanocomposite material (porous TiO$_2$ film - see Fig. 27).
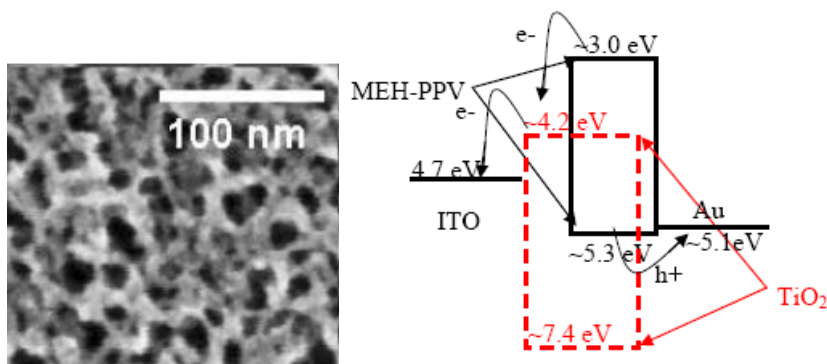

Fig. 27. SEM image of highly porous TiO2 layers consisting of a 3D interconnected network of anatase crystallites used for device fabrication. Right - Energy diagram of ITO/TiO2/MEH-PPV/Au.

With the control of the nanostructured morphology, metal oxides are believed to act as promising alternatives as the electron acceptor and transporter in bulk-heterojunction solar cells. Among the metal oxides, TiO$_2$ is a very good candidate for this purpose because the use of nanocrystalline TiO$_2$ as electron accepting electrode for dye-sensitized solar cells has shown an overall power conversion efficiency as high as 10%.

Mesoporous TiO$_2$ films were deposited on conducting glass ITO or SnO$_2$. By varying the temperature in the nanoparticle synthesis, the average particle diameter was altered between 20.5 and 41.5 nm. XRD measurements indicate that the TiO$_2$ particles were pure anatase within the detection limit of 3%–5%. Also, transmission electron microscopy indicates that the particles were crystalline. The film porosity was 57.5%±1.5% and was independent of the average particle size [64]. If to use MEH-PPV polymer as a p-type semiconductor, reported maximum EQE is 6%, short circuit current density - 0.4 mA/cm2 and power conversion efficiency - 0.17% under 100 mW/cm2 white light illumination [65].

Takahashi et al. [66] reported short circuit current density of 0.35 mA/cm² and power conversion efficiency of 0.13% under the irradiation of AM 1.5 illumination (100 mW/cm²). The short circuit current could be improved by about 3 times and power conversion efficiency could reach 0.47% by blending MEH-PPV with [2- [2- [4- (dimethylamino) phenyl]–ethenyl] -6- methyl -4H- pyran –4– ylidene] propanedinitrile (DCM). All results are comparable to same received with carbon based nanocomposites described above.

6. Conclusion

At present time application of semiconductor nanoparticles in different devices like solar sell and light emitting devices is a reality. However there are some problems connected with low value of charge carrier mobility and high exciton dissipation energy in disperse nanocomposite material. This problem can be solved by following way:
- augmentation of nanoparticles concentration in nanocomposite for preparation of hybrid material in which charge carrier transportation go over nanoparticles and not polymer matrix. Limitation: loss of flow proprieties and hence loss of good processability of material. Maximal level of nanoparticles concentration is limited in 20 - 25 vol % of nanoparticles concentration. This value is enough for charge carrier transport.
- formation of nanostructure in material layer to provide directed charge carrier transport between electrodes with minimal path length. This can be made by nanoimprint or self assembly methods. At present time there are the first examples of these nano- ordered structures.
Both problems can be solved and nanocomposite materials go to factory scale use application. For example, in conference (7-th International Conference ELECTRONIC PROCESSES IN ORGANIC MATERIALS (ICEPOM-7) Ukraine, Lviv, May 26 – 30, 2008 was being announced plastic nanostructured solar sell as a new product for commercial production since 2009: T. Yoshida, M. Matsui, K. Funabiki, H. Miura, Y. Fujishita Plastic solar cells employing electrodeposited nanostructured zno and organic photosensitizer, developed by Center of Innovative Photovoltaic Systems (CIPS), Gifu University, Yanagido, Japan. These results were published in the work [67].

7. References

1. A. Eychmu, J. Phys. Chem. B 104, 6514 (2000)
2. R. Rossetti, J. L. Ellison, J. M. Gibson and L. E. Brus, J. Chem. Phys. 80, 4464 (1984)
3. M. W. Peterson, M. T. Nenadovic, T. Rajh, R. Herak, O. Micic, J. P. Goral and A. J. Nozik, J. Phys. Chem. 92, 1400 (1988)
4. M. S. El-Shall, W. Slack, W. Vann, D. Kane and D. Hanley, J. Phys. Chem. 98, 3067 (1994), I. Yu. Denisyuk, T. R. Williams and J. Ed. Burunkova, Mol. Cryst. Liq. Cryst., 497, (2008.)
5. Ashfaq Adnan, C.T. Sun, Hassan Mahfuz A molecular dynamics simulation study to investigate the effect of filler size on elastic properties of polymer nanocomposites // Composites Science and Technology 67 (2007) 348–356
6. Odegard GM, Clancy TC, Gates TS. Modeling of the mechanical properties of nanoparticle/polymer composites. Polymer 2005; 46(2) p. 553–62.

A review of high nanoparticles concentration
composites: semiconductor and high refractive index materials
141

7. Binder K. Monte carlo and molecular dynamics simulations in polymer science. New York (USA): Oxford University Press; 1995.

8. C. Lu , Z. Cui, Z. Li, B. Yang and J. Shen, J. Mater. Chem., 13, 526 (2003)

9. J. H. Golden, H. Deng, F. J. DiSalvo, J. M. J. Fre´chet and P. M. Thompson, Science, 268, 1463 (1995)

10. J. H. Golden, F. J. DiSalvo, J. M. J. Fre´chet, J. Silcox, M. Thomas and J. Elman, Science, 273, 782 (1996)

11. C. Gao, B. Yang and J. Shen, J. Appl. Polym. Sci., 75, 1474 (2000)

12. P. Barbaro, C. Bianchini, G. Scapacci, D. Masi and P. Zanello, Inorg. Chem., 33, 3180 (1994)

13. Igor Yu. Denisyuk, Todd R. Williams, Julia E. Burunkova Hybrid optical material based on high nanoparticles concentration in UV-curable polymers – technology and proprieties // Mol. Cryst. Liq. Cryst., Vol. 497, pp. 142–153, 2008

14. Todd R. Williams, Igor Yu. Denisyuk, Julia E. Burunkova Filled polymers with high nanoparticles concentration – synthesis, optical and rheological proprieties // Journal of Applied Polymer Science, Volume 116 Issue 4, P. 1857 - 1866, 2010

15. H. Ishii, K. Sugiyama, E. Ito, and K. Seki, Adv. Mater. 11, 605 (1999)

16. J. M. Nunzi, C. R. Physique, 3, 523 (2002)

17. C. Kittel, Introduction à la physique de l'état solide, Bordas, Paris, (1972)

18. C. Cojan, G.P. Agrawal and C. Flytzanis, Phys. Rev. B, 15, 909, (1977)

19. J. Lange and H. Bässler, Phys. Stat. Sol. B, 114, 561 (1982)

20. J.H. Schön, C. Kloc, A. Dodabalapur and B. Batlogg, Science, 289, 599 (2000)

21. M. Schott and C. R. Acad. Sci. Paris Sér., 4, 381 (2000)

22. D. Emin, in Handbook of Conducting Polymers, edited T.A. Skotheim, M. Dekker, (1996), Vol. 2. p.

23. W.D. Gill, in Photoconductivity and Related Phenomena edited J. Mort, D.M. Pai, Elsevier, (1976) p. 63.

24. R.G. Kepler, P.M. Beeson, S.J. Jacobs, R.A. Anderson, M.B. Sinclair, V.S. Valencia and P.A. Cahill, Appl. Phys. Lett., 66, 3618 (1995)

25. G. Horowitz, Adv. Mater., 10, 365 (1998).

26. P.W.M. Blom, M.J.M. De Jong and J.J.M. Vleggaar, Appl. Phys. Lett., 68, 3308 (1996)

27. H.C.F. Martens, J.N. Huiberts and P.W.M. Blom, Appl. Phys. Lett., 77, 1852 (2000)

28. H. Scher, in Photoconductivity and Related Phenomena edited J. Mort, D.M. Pai, Elsevier, (1976) p. 63

29. M.N. Bussac and L. Zuppiroli, Phys. Rev. B, 55, 15587 (1997)

30. J.H. Schön, C. Kloc, R.C. Haddon and B. Batlogg, Science, 288, 656 (2000)

31. J.H. Schön, S. Berg, C. Kloc and B. Batlogg, Science, 287, 1022 (2000)

32. G.G. Malliaras, Y. Shen, D.H. Dunlap, H. Murata and Z.H. Kafafi, Appl. Phys. Lett., 79, 2582 (2001)

33. A.R. Inigo, C.H. Tan, W. Fann, Y.-S. Huang, G.-Y. Perng and S.-A. Chen, Adv. Mater., 13, 504 (2001)

34. C. Sentein, C. Fiorini, A. Lorin and J.M. Nunzi, Adv. Mater., 9, 809 (1997)

35. H. Murata, G.G. Malliaras, M. Uchida, Y. Shen and Z.H. Kafafi, Chem. Phys. Lett., 339, 161 (2001)]

36. H. Spanggaard and F. Krebs, Solar Energy Materials & Solar Cells, 83, 125 (2004)

37. J.H. Burroughes, D.D.C. Bradley, A.R. Brown, R.N. Marks, K. Mackay, R.H. Friend, P.L Burns and A.B. Holmes, Nature, 34, 539 (1990)

38. U. Rauscher, H. B.assler, D.D.C. Bradley and M. Hennecke, Phys. Rev. B, 42, 9830 (1990)
39. E.L. Frankevich, A.A. Lymarev, I. Sokolik, F.E. Karasz, S. Blumstengel, R.H. Baughman and H.H. Horhold, Phys. Rev. B, 46, 9320 (1992)
40. L.J. Rothberg, M. Yan, F. Papadimitrakopolous, M.E. Galvin, E.W. Kwock and T.M. Miller, Synth. Met., 80, 41 (1996)
41. T. Jerankoa, H. Tributscha, N.S. Sariciftcib and J.C. Hummelen, Solar Energy Materials & Solar Cells, 83, 247 (2004)
42. Md.K.H. Bhuiyan and T. Mieno, Thin Solid Films, 441, 187 (2003)
43. N.S. Sariciftci, D. Braun, C. Zhang, V.I. Srdanov, A.J. Heeger, G. Stucky and F. Wudl, Appl. Phys. Lett., 62, 585 (1993)
44. G. Yu, K. Pakbaz and A.J. Heeger, Appl. Phys. Lett., 64, 3422 (1994)
45. J.C. Hummelen, B.W. Knight, F. LePeq, F. Wudl, J. Yao and C.L. Wilkins, J. Org. Chem., 60, 532 (1995)
46. G. Yu, J. Gao, J.C. Hummelen, F. Wudl and A.J. Heeger, Science, 270, 1789 (1995)
47. S.E. Shaheen, C.J. Brabec, N.S. Sariciftci, F. Padinger, T. Fromherz and J.C. Hummelen, Appl. Phys. Lett., 78, 841 (2001)
48. U. Stalmach, B.d. Boer, C. Videlot, P.F.v. Hutten and G. Hadziioannou, J. Am. Chem. Soc., 112, 5464 (2000)
49. E. Peeters, P.A.v. Hal, J. Knol, C.J. Brabec, N.S. Sarciftci, J.C. Hummelen and R.A.J. Janssen, Phys. Chem. B., 104, 10174 (2000)
50. P.A. van Hal, J. Knol, B.M.W. Langeveld-Voss, S.C.J. Meskers, J.C. Hummelen and R.A.J. Janssen, J. Phys. Chem. A., 104, 5974 (2000)
51. F.C. Krebs, M. Jørgensen, Macromolecules, 35, 7200 (2002)
52. A. Cravino and N.S. Sariciftci, J. Mater. Chem., 12, 1931 (2002)
53. T. Benincori, E. Brenna, F. Sannicol, L. Trimarco and G. Zotti, Angew. Chem., 108, 718 (1996)
54. A. Cravino, G. Zerza, M. Maggini, S. Bucella, M. Svensson, M.R. Andersson, H. Neugebauer, C.J. Brabec and N.S. Sariciftci, Monatsh. Chem., 134, 519 (2003)
55. F.C. Krebs and M. Jørgensen, Polym. Bull., 50, 359 (2003)
56. P. V. Kamat, Nanotoday, 4, 315 (2006)
57. Y. Zhang, , and S. Iijima , Phys. Rev. Lett., 82, 3472(1999)
58. M. Freitag, Nano Lett., 4, 1063(2004)
59. Y.-Z. Ma, J. Chem. Phys., 120, 3368 (2004)
60. C. L.Kane, and E. Mele, J., Phys. Rev. Lett., 90, 207401(2003)
61. L. Sheeney-Haj-Ichia, Angew. Chem. Int. Ed. 44, 78 (2004)
62. I. Robel, Adv. Mater., 17, 2458(2005)
63. S. Hotchandani, and P. Kamat, J. Phys. Chem., 96, 6834 (1992)
64. N. Kopidakis, N. R. Neale, K. Zhu, J. van de Lagemaat, and A. J. Frank Appl. Phys. Lett., 87, 202106 (2005)
65. P. M. Sirimanne, T. Shirata, L. Damodare, Y. Hayashi, T. Soga, T. Jimbo, Solar Energy Materials and Solar Cells, 77, 15 (2003)
66. K. Takahashi, K. Seto, T. Yamaguchi, J.-I. Nakamura, C. Yokoe, and K. Murata, Chem. Lett. 33, 1042 (2004)
67. T. Dentania, K. Nagasakaa, K. Funabikia, J. Jinb, T. Yoshidac, H. Minourac and M. Matsui, Dyes and Pigments 77, Issue 1, (2008), 59-69
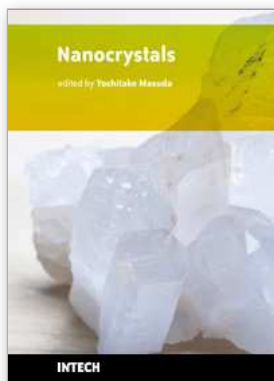
Nanocrystals

Edited by Yoshitake Masuda

This book contains a number of latest research developments on nanocrystals. It is a promising new research area that has received a lot of attention in recent years. Here you will find interesting reports on cutting-edge science and technology related to synthesis, morphology control, self-assembly and application of nanocrystals. I hope that the book will lead to systematization of nanocrystal science, creation of new nanocrystal research field and further promotion of nanocrystal technology for the bright future of our children.

How to reference

In order to correctly reference this scholarly work, feel free to copy and paste the following:

Igor Denisyuk and Mari Fokina (2010). A Review of High Nanoparticles Concentration Composites: Semiconductor and High Refractive Index Materials, Nanocrystals, Yoshitake Masuda (Ed.), ISBN: 978-953-307-126-8, InTech, Available from: http://www.intechopen.com/books/nanocrystals/high-nanoparticles-concentration-composites-semiconductor-and-high-refractive-index-materials

INTECH
open science | open minds